Study of electron-electron and electron-hole interactions in graphene interfaces of $G/SrTiO_3$ and $G/LaAlO_3$ using spectroscopy ellipsometry (SE)

By

Tay Shengyu

A0072549X

Supervisor

Assistant Professor Andrivo Rusydi

Co-Supervisor

Dr Pranjal Kumar Gogoi

National University of Singapore

A thesis submitted to the Faculty of Science as a Partial Fulfillment

of

the Bachelor of Science (Hons.) in Physics

2014

ACKNOWLEDGEMENTS

I would like to thank everybody who has assisted me over the past one year in my FYP project. I wish to begin by thanking Assistant Professor Andrivo Rusydi for giving me the chance to work under him in the Singapore Synchrotron Light Source (SSLS). It is a great honor to be part of this group. I would like to give my deepest gratitude for his continuous encouragement and guidance throughout the year as well as the numerous stimulating insights he has shed light on.

I also would like to sincerely thank my Co-Supervisor Dr. Pranjal Gogoi for his indispensable support and assistance throughout the year. There were many times we felt indebted because of our endless consultations and discussions with him and he was always most willing to impart his knowledge to us despite his busy schedule.

Needless to say, I would also like to thank Mr. Tan Ee Cheng, who has been my buddy at work, working on a similar FYP project as me. There were many difficult times which I felt stuck during this past year which he has helped me overcome. His assistance was invaluable as we were able to have many discussions and debates regarding our project work.

I also had like to thank the other members of the group whom we sought help upon when Asst. Prof Andrivo and Dr. Gogoi were not around as well as their encouragement and support throughout the year. Also, not forgetting my other friends and peers in the Physics department, for their continuous help and companionship throughout my undergraduate course.

Last but not least, I would like to thank my nearest and dearest family for their support as well as faith in me.

ABSTRACT

Graphene possesses novel mechanical, electrical, optical and thermal properties which make it a very viable candidate for device applications. However, being a 2D material, it cannot be used by itself and requires some sort of substrate for it to be applicable in most devices. In this thesis, we employ the use of Spectroscopic Ellipsometry to probe the optical conductivity (0.5-6.3eV) of graphene to study the interaction with which graphene has with its substrate at room temperature. We will be using 2 different substrates to present the substrate dependence of graphene- Strontium Titanate ($SrTiO_3$) and Lanthanum Aluminate ($LaAlO_3$). The study of the interaction at the interface will help better understand the suitability of the sample for device applications.

Our results show very strong interactions between Strontium Titanate ($SrTiO_3$) and graphene causing the band structure of graphene to change significantly. The results of the extracted graphene sheet conductivity show several new characteristics such as the occurrence of a new peak as well as UV transparency.

In the case of Lanthanum Aluminate ($LaAlO_3$) and graphene, we see a different kind of interaction from $SrTiO_3$ as a substrate as we see the universal value of the sheet conductivity of graphene increase from $\pi e^2/2h$ to $4\pi e^2/2h$ whilst retaining its peak at 4.6eV as in the case of free standing graphene.

In both cases, asymmetry of the optical spectra is observed, characteristic of Fano resonance. The presence of the resonant excitons in both cases exhibit low lifetime, which if we are able to put into device applications, can tremendously improve the frequency and hence speed of MOSFET devices.

Table of contents

List of Figures

Chapter One: Introduction

Ellipsometry is a widely used technique for thin film characterization. It is highly accurate due to the fact that it is self-normalizing. This means that only the intensity modulation is required and hence is able to avoid uncertainties coming from the fluctuations in the intensity of the light source. In ellipsometry, the principles are based on how the sample interacts with a linearly-polarized light as a probe, hence changing the p- and s-polarized light's amplitude and phase giving an elliptically-polarized light as an output which will be measured. In this chapter, we will provide an introduction to the principles of electromagnetism, optics and ellipsometry so as to facilitate the reader into comprehending the contents in subsequent chapters.

As a foreword, it would also be good to note that the definitions of some optical constants are different in optics and physics readings. Therefore, we will try to be consistent throughout this thesis and will be using the optics convention to define our optical constants.

1.1. Principles of electromagnetism and optics

Electromagnetic waves always travel at the speed of light, c, regardless of its wavelength and also obey the Maxwell's equations. They are composed of 2 one-dimensional transverse waves of **E** and **B** which are mutually perpendicular. For references, the Maxwell's equations can be found in the appendices.

In general, the propagation of a wave in one-dimension can be expressed in terms of a general wave expression at (x,t) by

$$\varphi = A\exp[i(\omega t - Kx + \delta)] \qquad (1.1)$$

Where A is the wave amplitude, K is the propagation number, ω is the angular frequency and δ is the initial phase of the wave. This can be brought forward to define our one-dimensional waves of **E** and **B** accordingly

$$E = E_0\exp[i(\omega t - Kx + \delta)] \qquad (1.2)$$
$$B = B_0\exp[i(\omega t - Kx + \delta)] \qquad (1.3)$$

In principle, there are 3 kinds of interactions that can occur as light is incident on a material surface. Light can be reflected, transmitted or absorbed by the material. Based

on the conservation of probability that the light which is incident on a material must go through either one of these interactions then gives that

$$R + T + \alpha = 1 \qquad (1.4)$$

Where R is the reflection coefficient, T is the transmission coefficient and α is the absorption coefficient.

As light is transmitted through a transparent medium, it gets refracted (bent) at the surface due to a change in its speed. The degree of refraction (bending) can be understood from the definition of the refractive index of a medium, *n*.

$$n = \frac{c}{v} \qquad (1.5)$$

where v is the speed of light in the medium. In vaccum, n is known be approximately 1. The degree of refraction of light travelling from medium 1 through 2 and their refractive indexes, n_1 and n_2, are related by Snell's law.

$$n_1 \sin\theta_1 = n_2 \sin\theta_2 \qquad (1.6)$$

where θ_1 is the angle of incidence and $\theta_2$is the angle of refraction.

More generally, in a non-transparent medium where a portion of light is absorbed by the medium as well, the behavior of light is better expressed by the complex refractive index, N.

$$N = n - ik \qquad (1.7)$$

where k (k≥0) is the extinction coefficient and is related to the absorption of light in a medium as will be shown in Eq. (1.10).

By substituting Eq. (1.6) into Eq. (1.2), we see that

$$E = E_0 \exp\left(-\frac{2\pi k}{\lambda}x\right)\exp[i\left(\omega t - \frac{2\pi n}{\lambda}x + \delta\right)] \qquad (1.8)$$

This shows that in a light-absorbing medium, the amplitude of the electric field actually decreases as an exponential function, $\exp(-2\pi kx/\lambda)$. That is, as the light gets transmitted deeper in the x direction into medium, its intensity decays as the light gets absorbed.

The intensity of light is then given by

$$I = |E|^2 = |E_0|^2 \exp\left(-\frac{4\pi k}{\lambda}x\right) \quad (1.9)$$

This is directly related to the Beer's law which states that

$$I = I_0 \exp(-\alpha d) \quad (1.10)$$

Where α is the absorption coefficient and d is the distance from the medium's surface.

It is easy to see that by comparing Eq. (1.8) and (1.9) that

$$\alpha = \frac{4\pi k}{\lambda} \quad (1.11)$$

This equation relates the absorption and extinction coefficient of a medium to be directly proportional to each other. If the medium is transparent, then α=k=0 and the intensity amplitude does not decay. That is, the light is either reflected or transmitted through.

1.2. Dielectric response of a medium

Considering a linear isotropic dielectric medium, the dielectric polarization of the medium is given as

$$P = \varepsilon_0 \chi E \quad (1.12)$$

Where ε_0 is the free-space permittivity and χ is the dielectric susceptibility.

The electric displacement, **D,** is related to the dielectric polarization, **P,** and **E** by

$$D = \varepsilon_0 E + P \quad (1.13)$$

By putting Eq. (1.11) and (1.12) together, we can hence show that

$$D = \varepsilon_0(1 + \chi)E \quad (1.14)$$

By definition, we also know that for a dielectric material,

$$D = \varepsilon_p E \quad (1.15)$$

Where ε_p is the permittivity of the dielectric medium.

Therefore giving us finally the relative dielectric response constant, ε, of a medium to be

$$\varepsilon = \frac{\varepsilon_p}{\varepsilon_0} = 1 + \chi = 1 + \frac{P}{\varepsilon_0 E} = \varepsilon_1 - i\varepsilon_2 \quad (1.16)$$

Where ε_1 and ε_2 are just the real and imaginary parts of the dielectric constant.

It is also known from electromagnetism that the complex refractive index is defined to be related to the dielectric constant as such

$$N^2 = (n - ik)^2 = \varepsilon \quad (1.17)$$

From Eq. (1.15) and (1.16), we can then write ε_1 and ε_2 in terms of n and k.

$$\varepsilon_1 = n^2 - k^2 \quad (1.18)$$
$$\varepsilon_2 = 2nk \quad (1.19)$$

Similarly, by inverting the equations, we can also write n and k in terms of ε_1 and ε_2.

$$n = \left\{\frac{\varepsilon_1 + (\varepsilon_1{}^2 + \varepsilon_2{}^2)^{1/2}}{2}\right\}^{1/2} \quad (1.20)$$

$$k = \left\{\frac{-\varepsilon_1 + (\varepsilon_1{}^2 + \varepsilon_2{}^2)^{1/2}}{2}\right\}^{1/2} \quad (1.21)$$

It should be noted that thus far, we have treated the dielectric as a constant. This is only true for the case of a monochromatic wavelength of light as the dielectric response of a medium actually varies as a function of the frequency of light being used, ω. What we are interested in is the dielectric response of the material as a function of the wavelength of light, $\varepsilon(\omega)$. i.e. the dielectric function.

In the classical picture, we can model the dielectric polarization as the oscillation of springs. When the frequency of the incident light coincides with the natural frequency of the spring, we have a resonant absorption which corresponds to a peak ε_2. It is easy to understand this by looking at Eq. (1.18) where we see that the extinction coefficient and hence absorption coefficient is directly proportional to ε_2.

1.3. Fresnel equations in a 2-layered medium system (01 system)

In the discussion of reflection of incident light off a medium, we can consider 2 kinds of polarization: the p-polarization and s-polarization. In p-polarization, the electric field vectors oscillate in the plane of incidence, whereas for the s-polarization, they oscillate in the plane perpendicular to the plane of incidence.

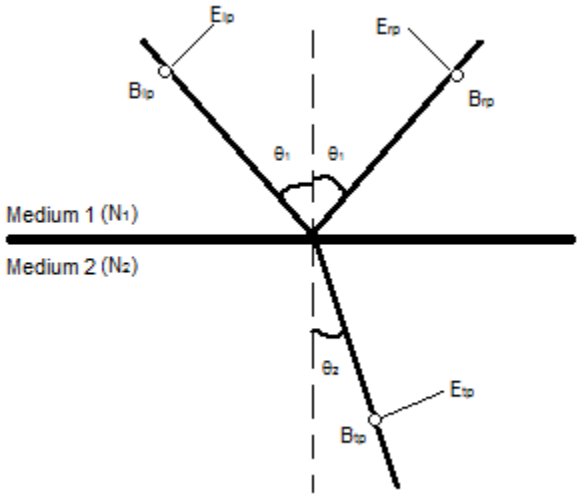

Figure 1.1: Reflection of p-polarized light

By solving the boundary conditions at the interface, such that the parallel components (p-polarization in this case) of the electric field and magnetic induction vectors must be continuous

$$E_{ip}\cos\theta_1 - E_{rp}\cos\theta_1 = E_{tp}\cos\theta_2 \quad (1.22)$$
$$B_{ip} + B_{rp} = B_{tp} \quad (1.23)$$

We can hence show the complex amplitude reflection coefficient and amplitude transmission coefficient for p-polarized light, r_p and t_p, to be

$$r_p = \frac{E_{rp}}{E_{ip}} = \frac{N_2\cos\theta_1 - N_1\cos\theta_2}{N_2\cos\theta_1 + N_1\cos\theta_2} \quad (1.24)$$

$$t_p = \frac{E_{tp}}{E_{ip}} = \frac{2N_1\cos\theta_1}{N_2\cos\theta_1 + N_1\cos\theta_2} \quad (1.25)$$

Similarly, we can solve for the s-polarized light boundary conditions

$$E_{is} + E_{rs} = E_{ts} \quad (1.26)$$
$$B_{rs}\cos\theta_1 - B_{is}\cos\theta_1 = -B_{ts}\cos\theta_2 \quad (1.27)$$

to give in the s-polarization,

$$r_s = \frac{E_{rs}}{E_{is}} = \frac{N_1\cos\theta_1 - N_2\cos\theta_2}{N_1\cos\theta_1 + N_2\cos\theta_2} \quad (1.28)$$

$$t_s = \frac{E_{ts}}{E_{is}} = \frac{2N_1\cos\theta_1}{N_1\cos\theta_1 + N_2\cos\theta_2} \quad (1.29)$$

The four equations above, Eq. (1.24), (1.25), (1.28) and (1.29) together give the Fresnel equations which describe the behavior of light moving through 2 mediums with different complex refractive indexes. These equations can be simplified by letting N_1=1 if we are performing an experiment in vacuum on a bulk substrate.

1.4. Fresnel equations in a 3-layered medium system (012 system)

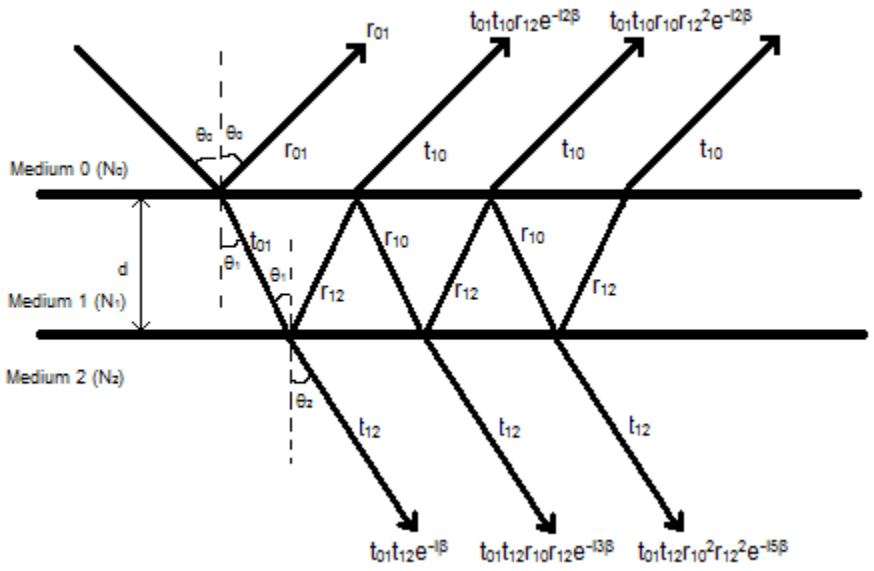

Figure 1.2: Optical model of a 3-layered medium system depicting the light's behavior.

Bringing forward the Fresnel equations in a 2-layered medium system to a 3-layered medium system, we can hence derive the Fresnel equations for the latter. We see that for an incident wave on such a system, the reflected light at the Medium 1 surface will meet with the light wave which had reflected at the Medium 1/2 interface, leading to an optical interference dependent on the phase difference between these waves. The phase difference between the 2 waves is given by

$$\alpha = \frac{4\pi d}{\lambda} N_1 \cos\theta_1 = 2\beta \qquad (1.30)$$

where we simply used β for redefining purposes, and β is commonly known as the film phase thickness. The resultant secondary reflected wave after multiplying by the amplitude coefficients is therefore given by $t_{01}t_{10}r_{12}e^{-i2\beta}$.

We see that in Figure 1.2, the amplitude reflection coefficient for the whole system is therefore a summation of the primary and secondarily reflected light waves.

$$r_{012} = r_{01} + t_{01}t_{10}r_{12}e^{-i2\beta} + t_{01}t_{10}r_{10}{r_{12}}^2e^{-i4\beta} + t_{01}t_{10}{r_{10}}^2{r_{12}}^3e^{-i6\beta} \ldots \qquad (1.31)$$

This is simply an infinite geometric series $\left(\sum_{k=0}^{\infty} ar^k = \frac{a}{1-r}\right)$ with the results of

$$r_{012} = r_{01} + \frac{t_{01}t_{10}r_{12}e^{-i2\beta}}{1 - r_{10}r_{12}e^{-i2\beta}} = \frac{r_{01} + r_{12}e^{-i2\beta}}{1 + r_{01}r_{12}e^{-i2\beta}} \quad (1.32)$$

Similarly, the transmission coefficient can be given by

$$t_{012} = \frac{t_{01}t_{12}e^{-i\beta}}{1 + r_{01}r_{12}e^{-i2\beta}} \quad (1.33)$$

The Fresnel equations derived in 1.32 and 1.33 form the basis of a ambience/film/substrate system which will later aid us in our understanding of the mechanics of optical experiments such as ellipsometry.

1.5. Principles of ellipsometry

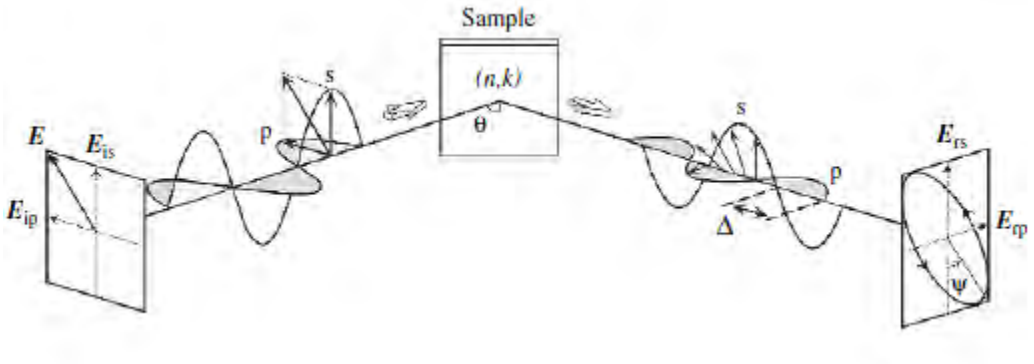

Figure 1.3: Simplified diagram showing measurement in ellipsometry [1]

Ellipsometry makes use of incident light of a known polarization on a sample. Due to interaction at the surface/interface of the sample, the known polarization of the incident light then changes. The change in the polarization and amplitude reflection coefficient is then measured by a light detector. Usually, as it is in the case of our experiment, a linearly polarized light is set incident on the sample. Then, due to the interaction with the sample, the light undergoes a phase and amplitude change between the p- and s-polarized light. This hence leads to an elliptically polarized light being detected at the output.

There are 2 parameters which describe the output polarization (ψ,Δ), which are the amplitude ratio and phase difference between the output p- and s-polarized light as shown in Figure 1.3. The measurement of (ψ,Δ) for each wavelength can then give us the frequency dependent (n,k) of our sample by applying the Fresnel equations.

$$\rho = \tan\varphi\, e^{i\Delta} = \frac{r_p}{r_s} = \frac{\left(\frac{E_{rp}}{E_{ip}}\right)}{\left(\frac{E_{rs}}{E_{is}}\right)} \qquad (1.34)$$

It is easy to see that the ellipsometry parameters (ψ,Δ) describe the ellipticity of the output polarization as illustrated in Figure 1.4.

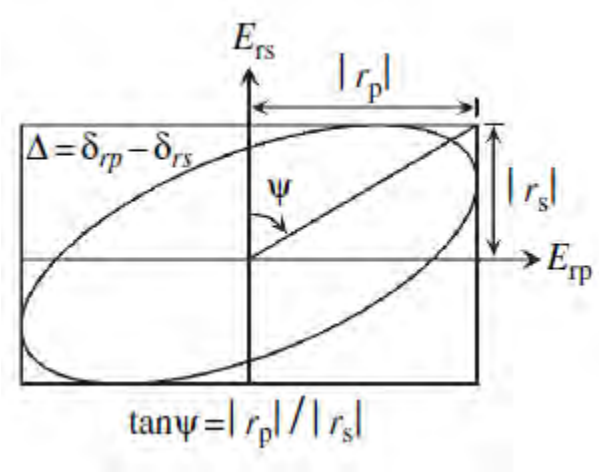

Figure 1.4: The physical meaning of (ψ,Δ) [1]

Ellipsometry in general uses a multitude of optical elements to help produce a known polarization as well as in the analysis of output polarization. Ellipsometry can be performed in various modes by varying the optical elements present in the experimental set up. For example, a polarizer may be placed at 45^0 just after the light source to produce a linear polarization, and a retarder just after to induce a phase difference between the p- and s-polarized light hence converting the linear polarization to a circular polarized light incident on the sample. In the rotating analyzer mode (RAE), a rotating analyzer is then employed at the end to help determine the ellipticity of polarization.

1.6. Jones matrix/vector

To help us understand the measurements in ellipsometry, it is important to understand the Jones matrix which gives a mathematical description of optical measurements. This means that the conversion of one polarization state to another may be mathematically described using a Jones matrix if we know the optical elements present in the

experimental set up. Typically, these polarization states are expressed in what we call Jones vectors.

For an electromagnetic wave travelling in the z-direction,

$$E(z,t) = \begin{bmatrix} E_x \\ E_y \end{bmatrix} \quad (1.35)$$

Where E_x and E_y are given as

$$E_x = E_{ox} e^{i\delta_x} \quad (1.36)$$
$$E_y = E_{oy} e^{i\delta_y} \quad (1.37)$$

And the light intensity can then be computed to be

$$I = I_x + I_y = |E_x|^2 + \left|E_y\right|^2 = E_x {E_x}^* + E_y {E_y}^* \quad (1.38)$$

Correspondingly, since we only take into account the relative changes in amplitude and phase in ellipsometry, the Jones vector is expressed by the normalized light intensity.

$$E_x = \begin{bmatrix} 1 \\ 0 \end{bmatrix} \quad E_y = \begin{bmatrix} 0 \\ 1 \end{bmatrix} \quad (1.39)$$

And for the linearly polarized light at +45°, the Jones vector hence becomes

$$E_{+45} = \frac{1}{\sqrt{2}} \begin{bmatrix} 1 \\ 1 \end{bmatrix} \quad (1.40)$$

Similarly, it is possible to give mathematical descriptions to right circular polarized light (E_R) and left circular polarized light (E_L) as well as elliptic polarized light ($E_{elliptic}$)

$$E_R = \frac{1}{\sqrt{2}} \begin{bmatrix} 1 \\ i \end{bmatrix} \quad E_L = \frac{1}{\sqrt{2}} \begin{bmatrix} 1 \\ -i \end{bmatrix} \quad (1.41)$$

$$E_{elliptic} = \begin{bmatrix} \sin\varphi e^{i\Delta} \\ \cos\varphi \end{bmatrix} \quad (1.42)$$

1.6.1 Jones matrix of polarizer/analyzer

A polarizer placed in front of the light source can convert unpolarized light to a linearly polarized light. An analyzer acts as the same function as a polarizer, except that it is placed in front of a light detector, and hence both of these optical elements share the same mathematical description/Jones matrix given below.

$$A = P = \begin{bmatrix} 1 & 0 \\ 0 & 0 \end{bmatrix} \quad (1.43)$$

1.6.2 Jones matrix of compensator/retarder

A compensator (retarder) can be placed behind a polarizer or in front of an analyzer to convert linearly polarized light to a circularly polarized light, vice versa. This is possible because the retarder acts to generate a phase difference between the E_x and E_y vectors.

$$C = \begin{bmatrix} 1 & 0 \\ 0 & e^{-i\delta} \end{bmatrix} \quad (1.44)$$

1.6.3 Jones matrix of an isotropic sample

An isotropic sample will also change the polarization state of light and therefore may be represented in the form of a Jones matrix as well.

$$S_p = \begin{bmatrix} r_p & 0 \\ 0 & r_s \end{bmatrix} = r_s \begin{bmatrix} r_p/r_s & 0 \\ 0 & 1 \end{bmatrix} \equiv \begin{bmatrix} \sin\varphi\, e^{i\Delta} & 0 \\ 0 & \cos\varphi \end{bmatrix} \quad (1.45)$$

There is a proportional constant which was neglected in Eq. (1.45) since ellipsometry only takes into account the relative changes.

1.7. Stokes vector/ Mueller matrix

There is a limit to which how much the Jones vector can describe. The Jones vector cannot describe unpolarized or partial polarization states. The Stokes vectors hence and should be used to describe all kinds of polarization states in ellipsometry. This is precisely what is being measured in an ellipsometry experiment. Contrary to the Jones matrix which describes the optical elements in the Jones representation, the Mueller matrix describes the optical elements in the Stokes vector representation.

The Stokes vector consists of 4 parameters ($S_{0\text{-}3}$) which can be expressed in terms of the intensities.

$$S_0 = I_x + I_y \quad (1.46)$$
$$S_1 = I_x - I_y \quad (1.47)$$
$$S_2 = I_{+45} - I_{-45} \quad (1.48)$$
$$S_3 = I_R - I_L \quad (1.49)$$

Here, the subscripts indicate the linear polarization state of the intensities and $S_{1\text{-}3}$ represent the relative difference in light intensity between each state of polarization. Together, these 4 parameters then give the Stokes vector, S.

$$S = \begin{bmatrix} S_0 \\ S_1 \\ S_2 \\ S_3 \end{bmatrix} \quad (1.50)$$

In the elliptical polarization, we may express the Stokes vector using the (ψ,Δ) coordinate system such as that illustrated in Figure 1.4 to give

$$S = \begin{bmatrix} 1 \\ -\cos 2\varphi \\ \sin 2\varphi \cos \Delta \\ -\sin 2\varphi \cos \Delta \end{bmatrix} \quad (1.51)$$

Similarly, the effect of optical elements on the polarization state can be represented in a matrix form. However, since the Stokes vector is a 4x1 vector, the matrix of the optical elements is now a 4x4 matrix.

1.7.1 Mueller matrix of fixed polarizer/analyzer

$$P = A = \frac{1}{2}\begin{bmatrix} 1 & 1 & 0 & 0 \\ 1 & 1 & 0 & 0 \\ 0 & 0 & 0 & 0 \\ 0 & 0 & 0 & 0 \end{bmatrix} \quad (1.52)$$

1.7.2 Mueller matrix of fixed compensator

$$C = \begin{bmatrix} 1 & 0 & 0 & 0 \\ 0 & 1 & 0 & 0 \\ 0 & 0 & \cos\delta & \sin\delta \\ 0 & 0 & -\sin\delta & \cos\delta \end{bmatrix} \quad (1.53)$$

1.7.3 Mueller matrix of isotropic sample

$$S_p = \begin{bmatrix} 1 & -\cos 2\varphi & 0 & 0 \\ -\cos 2\varphi & 1 & 0 & 0 \\ 0 & 0 & \sin 2\varphi \cos \Delta & \sin 2\varphi \sin \Delta \\ 0 & 0 & -\sin 2\varphi \sin \Delta & \sin 2\varphi \cos \Delta \end{bmatrix} \quad (1.54)$$

1.8. Data analysis in ellipsometry

In ellipsometry, the determination of the sample's optical constants is not known directly. The measured parameters of (ψ,∆) needs to be converted into the optical constants by constructing an optical model (in the case when the sample is of unknown dimensions) and modelling of the dielectric function. In this section, we will focus more on the modelling of the dielectric function since we will be performing ellipsometry under a known dimension sample.

There are many different models for the dielectric function, and it is necessary to choose an appropriate model which is characteristic of the sample to ensure a correct fitting.

1.8.1 Dielectric function model – Lorentz model

The Lorentz model is a classical model which models the electric polarization between electrons and the nucleus in the sample as a spring. The electron is modelled to oscillated about the fixed atomic nucleus, since its mass is much light than the latter. When light is incident upon, it will induce a dielectric polarization along the spring direction.

By Newton's 2nd law, assuming the modelled spring is along the x axis,

$$m_e \frac{d^2x}{dt^2} = -m_e \Gamma \frac{dx}{dt} - m_e {\omega_0}^2 x - eE_0 e^{i\omega t} \quad (1.55)$$

Where the first term comes from the viscous forces and Γ is the damping coefficient, the second term is the restoration force coming from Hooke's law, and the last term comes from the electrostatic force.

This 2nd order ODE can be solved by using the solution, $x(t) = a\, exp(\mathrm{i}\omega t)$. By substituting this solution into Eq. (1.55), we may then see that

$$a = -\frac{eE_0}{m_e}\frac{1}{({\omega_0}^2 - \omega^2) + i\Gamma\omega} \quad (1.56)$$

Using Eq.(1.16) and rewriting the dielectric polarization in terms of the number of electrons per unit volume N_e as $P = -eN_e x(t) = -eN_e a\, exp(i\omega t)$, we then get the dielectric constant as

$$\varepsilon = 1 + \frac{P}{\varepsilon_0 E} = 1 + \frac{e^2 N_e}{\varepsilon_0 m_e}\frac{1}{({\omega_0}^2 - \omega^2) + i\Gamma\omega} \quad (1.57)$$

And by further separating the real and imaginary parts,

$$\varepsilon_1 = 1 + \frac{e^2 N_e}{\varepsilon_0 m_e}\frac{({\omega_0}^2 - \omega^2)}{({\omega_0}^2 - \omega^2)^2 + \Gamma^2\omega^2} = 1 + {\omega_p}^2\frac{({\omega_0}^2 - \omega^2)}{({\omega_0}^2 - \omega^2)^2 + \Gamma^2\omega^2} \quad (1.58)$$

$$\varepsilon_2 = \frac{e^2 N_e}{\varepsilon_0 m_e}\frac{\Gamma\omega}{({\omega_0}^2 - \omega^2)^2 + \Gamma^2\omega^2} = {\omega_p}^2\frac{\Gamma\omega}{({\omega_0}^2 - \omega^2)^2 + \Gamma^2\omega^2} \quad (1.59)$$

where ω_p is the plasma frequency. In terms of the photon energy En, we can also re-express Eq. (1.57) as the sum of different oscillators giving

$$\varepsilon = 1 + \sum_j \frac{A_j}{{En_0}_j^2 - En^2 + i\Gamma_j En} \quad (1.60)$$

Where A_j is oscillator strength of the j[th] oscillator.

1.8.2 Dielectric function model – Sellmeier and Cauchy model

Depending on the sample, The Sellmeier or Cauchy model can also be used to model the dielectric function. The Sellmeier and Cauchy models both describe a sample/region where there is no absorption. i.e. $\varepsilon_2 = 0$.

For the Cauchy model,

$$n = A + \frac{B}{\lambda^2} + \frac{C}{\lambda^4} + \cdots, \qquad k = 0 \quad (1.61)$$

Where A, B and C are just empirical constants.

And for the Sellmeier model, which is a further development of the Cauchy, the dielectric function is expressed as

$$\varepsilon_1 = n^2 = A + \sum_j \frac{B_j \lambda^2}{\lambda^2 - {\lambda_{0j}}^2}, \qquad \varepsilon_2 = k = 0 \tag{1.62}$$

1.8.3 Dielectric function model – Drude model

The Drude model is accounts for the free carrier contribution to the dielectric function. It is capable of describing light absorption characteristic of free electrons in metals and free carriers in semiconductors.

The Drude model utilizes the classical equation of motion of electrons in an optical electric field to derive the dielectric function. Classically, this is given as

$$m\frac{d\vec{v}}{dt} + \frac{m\vec{v}}{\tau} = -eE_0 e^{i\omega t} \tag{1.63}$$

Where $\tau \equiv \Gamma^{-1}$ is the relaxation time and $\vec{v}$ is the drift velocity of the carrier.

Similar to how we solved this kind of equation for the Lorentz model, we may then obtain the dielectric function in the Drude model

$$\varepsilon = \varepsilon_\infty \left(1 - \frac{{\omega_p}^2}{\omega^2 - i\omega\Gamma}\right) \tag{1.64}$$

Where ε_∞ is the high frequency dielectric constant.

Once again, in terms of the photon energy En, we may rewrite Eq. (1.64) into

$$\varepsilon = \varepsilon_\infty - \frac{\varepsilon_\infty {E_p}^2}{En^2 - i\Gamma En} \tag{1.65}$$

1.8.4 Dielectric function model – Drude-Lorentz model

Typically, we may combine the Drude and Lorentz model together to fully describe the dielectric functions of metals and conductive semiconductors which has a contribution from the free carriers as well as from bound electrons. When used together, they allow us to describe ellipsometric data over a large spectral range.

$$\varepsilon(En) = \varepsilon_{FCA}(En) + \varepsilon_{bound}(En) = \varepsilon_{Drude}(En) + \varepsilon_{Lorentz}(En) \tag{1.66}$$

The free carrier absorption contribution is accounted for by the Drude model and the bound electrons contribution is accounted by the j Lorentz oscillators.

$$\varepsilon(En) = \varepsilon_{\infty} - \left(\frac{f_0 {E_p}^2}{En^2 - i\Gamma_0 En}\right) + \sum_j \frac{f_j {E_p}^2}{{En_j}^2 - En^2 + i\Gamma_j En} \qquad (1.67)$$

1.8.5 Data analysis procedure – Linear Regression Analysis

Linear regression analysis is one of the standard data analysis procedures used in ellipsometry. A fitting error function σ is plotted against analytical parameters such as layer thickness or dielectric model parameters to find out the optimal parameters where the fitting error may be minimized. The flow chart of such a data analysis procedure is shown below.

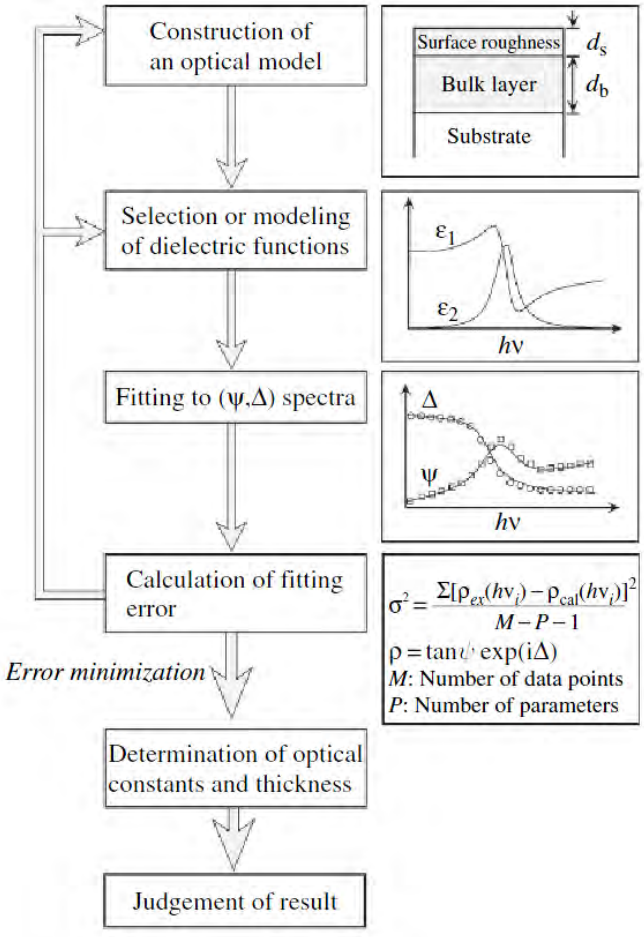

Figure 1.5: Flowchart of data analysis in ellipsometry adapted from [1]

An optical model of the sample is first constructed. For a bulk sample, this would be considered a 01 system as described in Section 1.3. For a thin film of bulk substrate, this would be a 012 system as described in Section 1.4. If the thickness of the sample is known, then it may be kept fixed, however, if it is not, then it may be used as one of the analytical parameters used to optimize the fitting error. A suitable dielectric function is then used to describe each layer. By varying the analytical parameters, the output (ψ,Δ) spectra is then fitted against our own experimental data. After a decent fitting, the fitting error function may then be calculated to see if we are capable of minimizing the error function even more by varying the parameters. When the fitting error is minimized, or within acceptable limits, we are said to have then extracted the required optical constants and thickness of the thin film.

The fitting error function we will be using for our data analysis will be the unbiased estimator or mean squared error (MSE) given by

$$\sigma^2 = \frac{1}{M-P-1}\sum_{j=1}^{M}\left\{\rho_{exp}(E) - \rho_{cal}(E)\right\}^2 \qquad (1.68)$$

Where M is the number of measurement points, P is the number of analytical parameters and

1.9. The Hilbert transform - Kramers-Kronig transformation

The Hilbert transform, H, arises from digital signal processing and allows us to relate the real and imaginary parts of a complex signal. Such a real and imaginary part is considered a Hilbert transform pair.

Consider a complex signal

$$z(\omega) = x(\omega) + iy(\omega) \qquad (1.69)$$

Where $x(t)$ and $y(t)$ are real functions.

From the definition of the Hilbert transform, we then get

$$y(\omega) = H\{x(\omega)\} = \frac{1}{\pi}P\int_{-\infty}^{\infty}\frac{x(\omega')}{\omega-\omega'}d\omega' \qquad (1.70)$$

$$x(\omega) = H^{-1}\{y(\omega)\} = -\frac{1}{\pi}P\int_{-\infty}^{\infty}\frac{y(\omega')}{\omega-\omega'}d\omega' \qquad (1.71)$$

Where P is the Cauchy principal value of the integral of when $u = \omega$.

The real and imaginary parts of the dielectric function, $\varepsilon_1$and ε_2, are one of such Hilbert transform pairs. Such a Hilbert transform relating $\varepsilon_1$and ε_2 is known as the Kramers-Kronig transformation. We understand that from Eq. (1.15), the dielectric function originates from a linear response function, and therefore satisfies the causality condition. This means that, intuitively as we already know, reflected light (or absorption) cannot appear before the light is incident upon the sample.

$$\varepsilon_1(\omega) = 1 + \frac{2}{\pi} P \int_0^{\infty} \frac{\omega' \varepsilon_2(\omega')}{\omega'^2 - \omega^2} d\omega' \qquad (1.72)$$

$$\varepsilon_2(\omega) = -\frac{2\omega}{\pi} P \int_0^{\infty} \frac{\varepsilon_1(\omega') - 1}{\omega'^2 - \omega^2} d\omega' \qquad (1.73)$$

This means that once either of the functions is known for all frequencies, the other is immediately known through this relation. It should be noted that Sellmeier and Cauchy models do not satisfy the Kramers-Kronig relation because they assume that there is no absorption in the region. This implies that $\varepsilon_2 = 0$ for all frequencies and if we substitute this into Eq. (1.72), we see that $\varepsilon_1(\omega)$ gives us a constant which should not be the case.

1.10. Excitons

In the study of electronic band structures, we may infer insights on the interactions between charge carriers. One such interaction would be the electron-hole interaction. In the interband transition where photons are absorbed, the electron is excited from the valence band to the conduction band leaving behind a hole. Excitons may be formed in such a system where the electron and hole are bound together as a pair by their Coulomb interaction. Provided that the energy (e.g. thermal) is to not large, the exciton may continue to reside within the crystal and hence have interesting effects on the optical properties of the sample as we shall see. If the temperature is high enough, thermally excited phonons may start to collide with the excitons and provide them with an energy greater than their binding energy and cause the exciton to dissipate.

In a simple physical picture, it is possible to model an exciton as a hydrogenic system although it should be taken note that the exciton binding energy is usually much smaller than that for a hydrogen atom because of the screening effects from neighboring electrons as well as their smaller effective mass.

Excitons can be classified into 2 general kinds: Wannier-Mott excitons which are free excitons, and Frenkel excitons which are bound excitons.

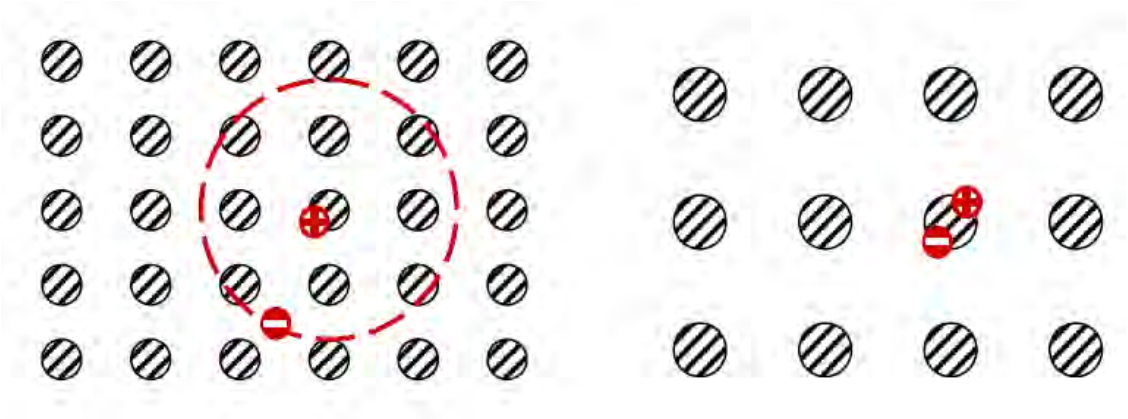

Figure 1.6: The Wannier-Mott exciton (left) and Frenkel exciton (right)

As Figure 1.6 illustrates, the Wannier exciton typically has a large radius (~100Å) as compared to the lattice spacing between atoms. This makes them delocalized states with a lower binding energy of about 0.01eV that are capable of moving freely about the crystal. Frenkel excitons on the other hand have a smaller radius (~10Å) with a higher binding energy of about 1eV. This radius is usually comparable to the size of the lattice spacing, hence making them a well localized state.

1.11. Strontium Titanate ($SrTiO_3$)

Strontium Titanate has is a transition metal oxide a perovskite cubic crystal structure. Perovskite oxides have a chemical formula of the kind ABO_3, where A and B are different cations. In this case, A is Strontium (Sr) and B is Titanium (Ti). Experimental findings show that it has a fundamental absorption edge of 3.2eV at room temperature and a direct band gap of 3.75eV [7].

It has a crystal structure as shown below with a cubic lattice constant of 3.905Å at room temperature [11]. There are many interesting properties regarding this material. One of it is that it undergoes an antiferrodistortive (AFD) phase transition at 110K [6,10]. Below this critical temperature, it transforms into the tetragonal structure.

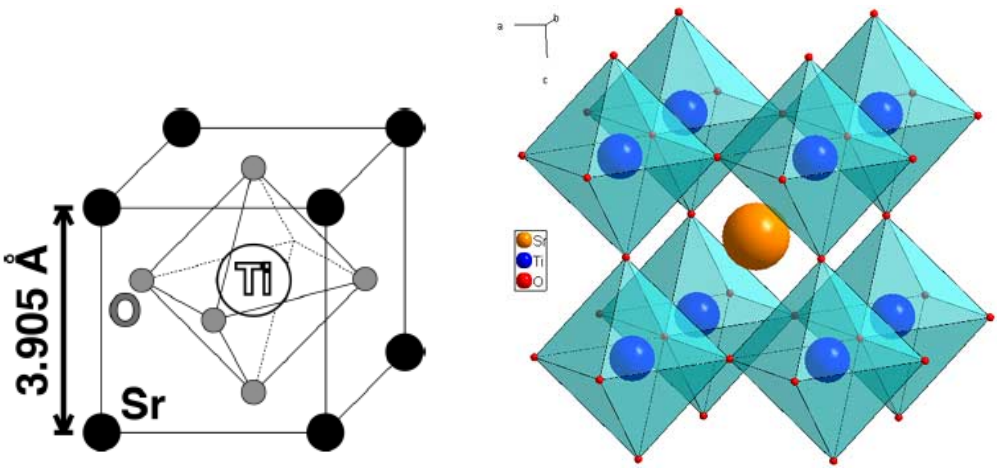

Figure 1.7a and b: Crystal structure of $SrTiO_3$ [6](left) and [9](right)

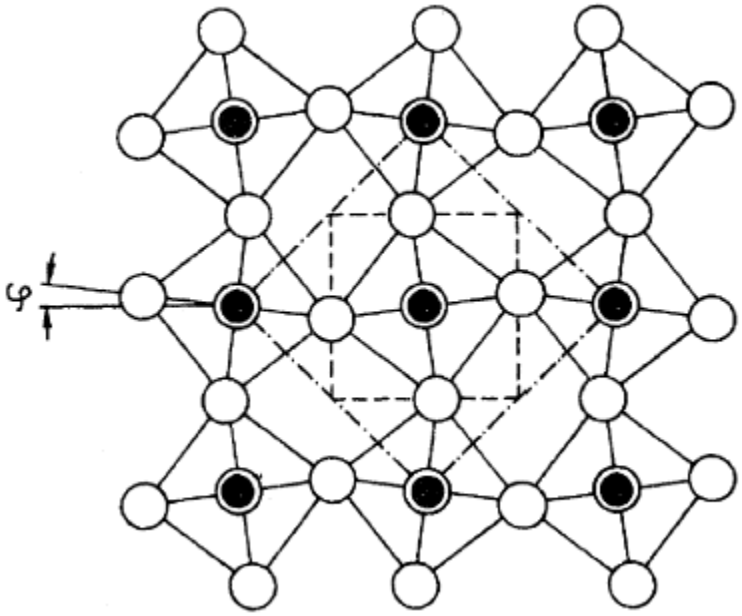

Figure 1.8: Schematic diagram showing the AFD phase transition in $SrTiO_3$ [12]

This AFD phase transition can be understood by the rotation of the oxygen octahedra in the xy-plane as seen in Figure 1.8. Figure 1.8 is a schematic diagram of the phase transition looking down the (001) direction. As the octahedra in the middle rotates anti-clockwise, the adjacent octahedra rotates clockwise. This results in an enlarged tetragonal unit cell as seen in the diagram.

Since Ti^{4+} is tetravalent, with 2 electrons from 3d and 4s shell each and Sr^{2+} is divalent with 2 electrons from the 5s shell, we can think of $SrTiO_3$ being built up from SrO and TiO_2 layers which result in a non-polar oxide.

As seen in Figure 1.7, the oxygen ions break the atomic spherical symmetry of Sr and Ti ions and hence removing the five-fold degenerate d levels.

The d orbitals may be distinguished into 2 subgroups based on their symmetry. These 2 subgroups are known as the t_{2g} and e_g group.

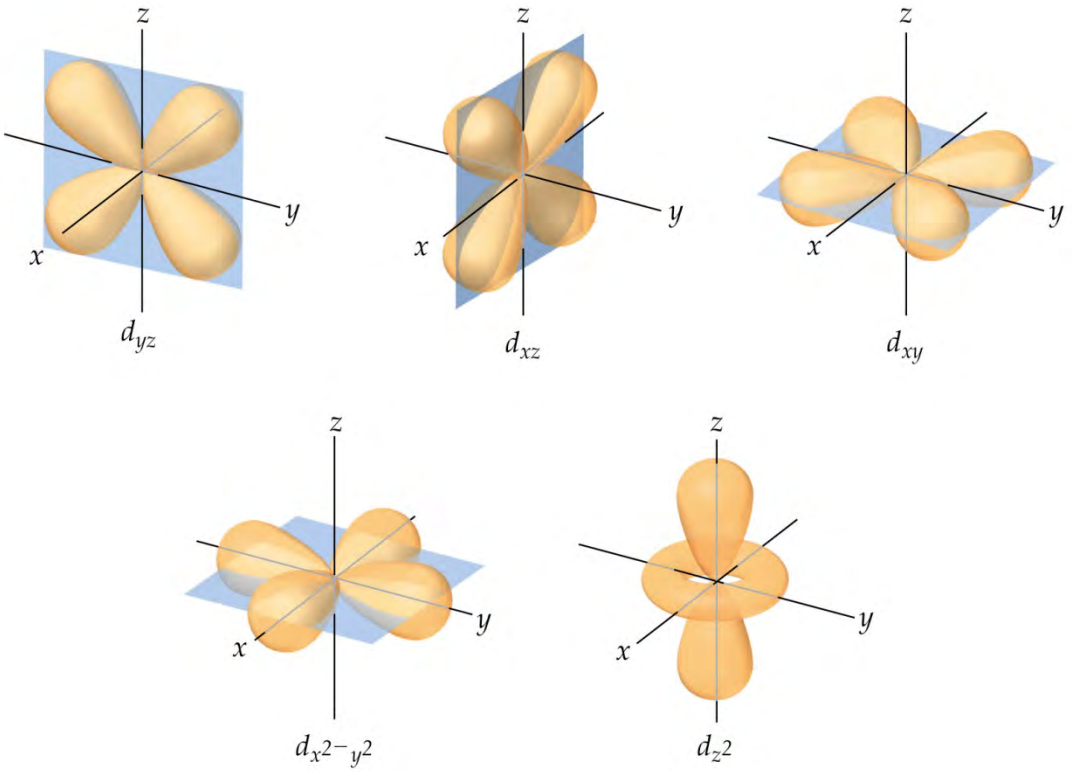

Figure 1.9: d orbitals separated into their 2 subgroups: t_{2g} (above) and e_g (below) [8]

As seen in Figure 1.7b, for Sr ions, they are surrounded by 12 O. This means that they are in dodecahedral symmetry.

Based on crystal field theory, the t_{2g} d-orbital group of Sr interacts more heavily (through repulsion based on the Pauli Exclusion Principle) with the 12 surrounding O ions, therefore raising their energy.

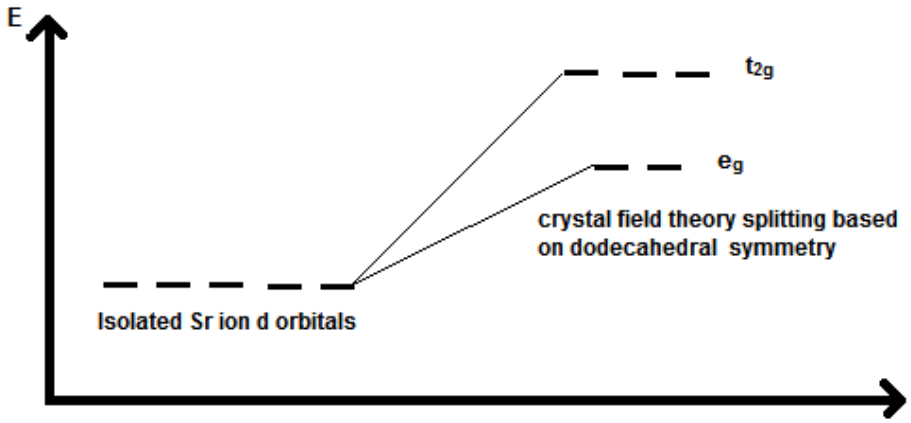

Figure 1.10: Crystal field splitting of Sr ion in dodecahedral symmetry

Therefore, as seen in Figure 1.10, the t_{2g} Sr 4d-orbitals are higher in energy than e_g Sr 4d-orbitals for the Sr ions.

As for Ti ions in Figure 1.7a, they are surrounded by 6 O giving them an octahedral symmetry. In this case, the e_g Ti 3d-orbitals are raised with respect to the t_{2g} Ti 3d-orbitals instead as deducible from crystal field theory once again.

It is also important to note that the O 2p orbitals which lie along the Cartesian axes will hybridize with the e_g Ti 3d-orbitals since they will have a spatial overlap. i.e. a hybridization between O $2p_z$ with Ti d_{z^2} and O $2p_{x,y}$ with Ti $d_{x^2-y^2}$.

1.11.1. Band structure of $SrTiO_3$

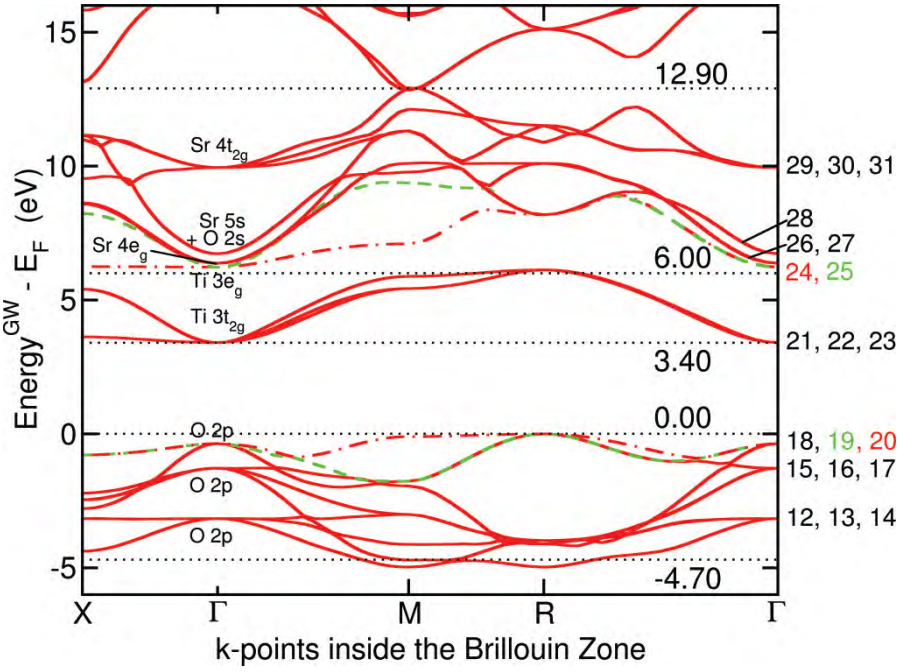

Figure 1.11: Band structure of $SrTiO_3$ calculated using LDA+G_0W_0 approximation by [6]

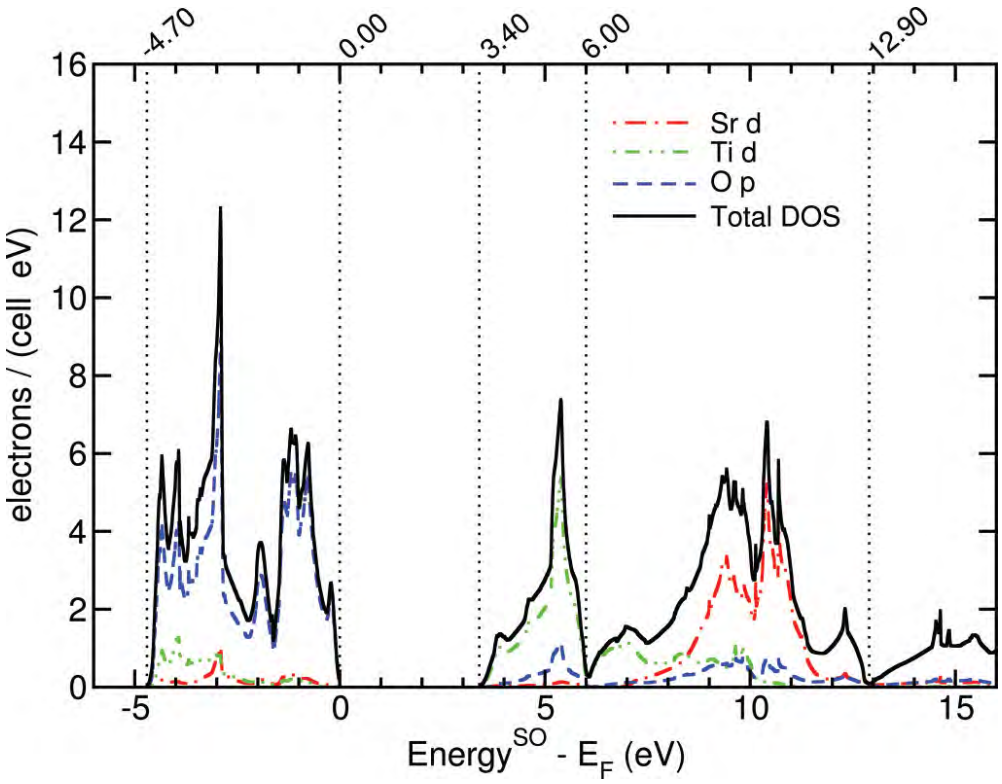

Figure 1.12: on-site angular momenta-projected *l*-DOS calculated by [6]

By using the results of Figure 1.12 we can assign the conduction/valence bands in Figure 1.11 to their respective orbitals based on their character. These results will help us extend our knowledge of knowing what kind of transitions is occurring at a particular energy range.

To begin the assignment of bands, Oxygen has a high electronegativity with respect to Strontium and Titanium, therefore we expect the Oxygen to attract most of the $3d^2$ and $4s^2$ from Ti and $5s^2$ electrons from Sr. This suggests a filling of the O 2p orbitals, leading us to assign the valence bands (-4.7eV to 0eV) to be composed of the O 2p states which also weakly hybridize with the Ti $3e_g$ states as mentioned earlier.[6]

From Figure 1.12, we can also see that the second band of structures (3.4eV to 6eV) is predominantly made up of Ti 3d character. Since we know from crystal field theory that the $3t_{2g}$ levels must be lower than the $3e_g$ level, we can hence assign bands (21-23) to Ti $3t_{2g}$ levels.[6]

Also with the help of Figure 1.12, we can assign to 2 lowest bands in the next band of structures (6-12.9eV) to the Ti $3e_g$ levels. Also from crystal field theory, we can assign bands (29-31) to Sr $4t_{2g}$ levels and band (26,27) to the Sr $4e_g$ levels. Also, according to [10], band 28 is due to the hybridization of Sr 5s orbitals with the O 2s orbitals.

1.12. Lanthanum Aluminate ($LaAlO_3$)

Lanthanum Aluminate is a perovskite with a similar crystal structure to $SrTiO_3$. As in Figure 1.7, the La ions now replace Sr and Al replaces Ti. Similar to $SrTiO_3$, it undergoes an AFD phase transition at 813K from a cubic to the rhombohedral-central hexagonal structure at room temperature. (R-3C space group) [21] The phase transition can be visualized by the rotation of the oxygen octahedra around the (111) axis and compressing them along this axis. [10] The rhombohedral lattice parameters are a=b=5.370Å and c=13.138Å. [21] But as the distortion from a cubic structure is not much (0.10^{o}), we can consider it to be a pseudo-cubic at room temperature with a lattice constant of 3.791Å. [10] $LaAlO_3$ is also known to have a large band gap of (5.5-6.5eV) [21]

Both La^{3+} and Al^{3+} which are trivalent contribute 3 electrons to form the covalent Al-O bonds. Hence we can think of the $LaAlO_3$ crystal as $(LaO)^{+}$ and $(AlO_2)^{-}$ layers alternatingly stacked making it a polar oxide. [10]

Since $LaAlO_3$ shares the same crystal structure as $SrTiO_3$, similar to how the Sr and Ti atoms were, the Al atoms are therefore at the body center of octahedral sites AlO_6 and La atoms are 12-fold coordinated by the O atoms.

1.12.1. Band structure of $LaAlO_3$

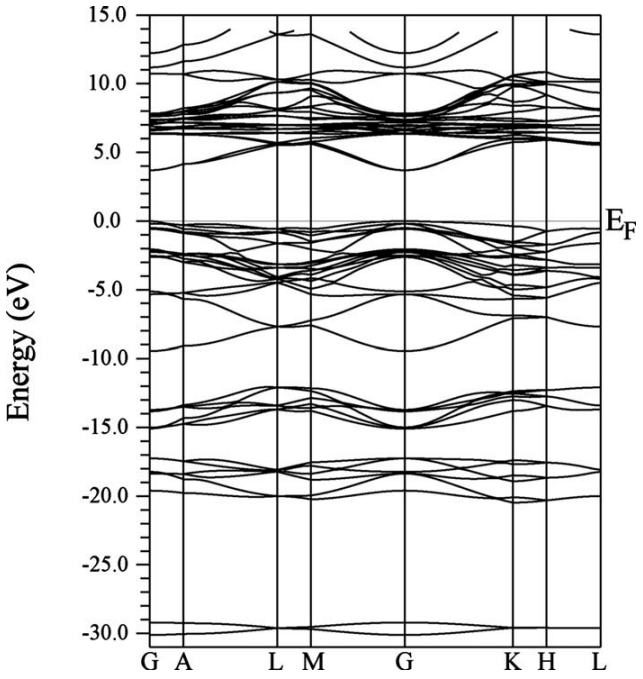

Figure 1.13: Band structure of rhombohedral LaAlO3 computed by [21]

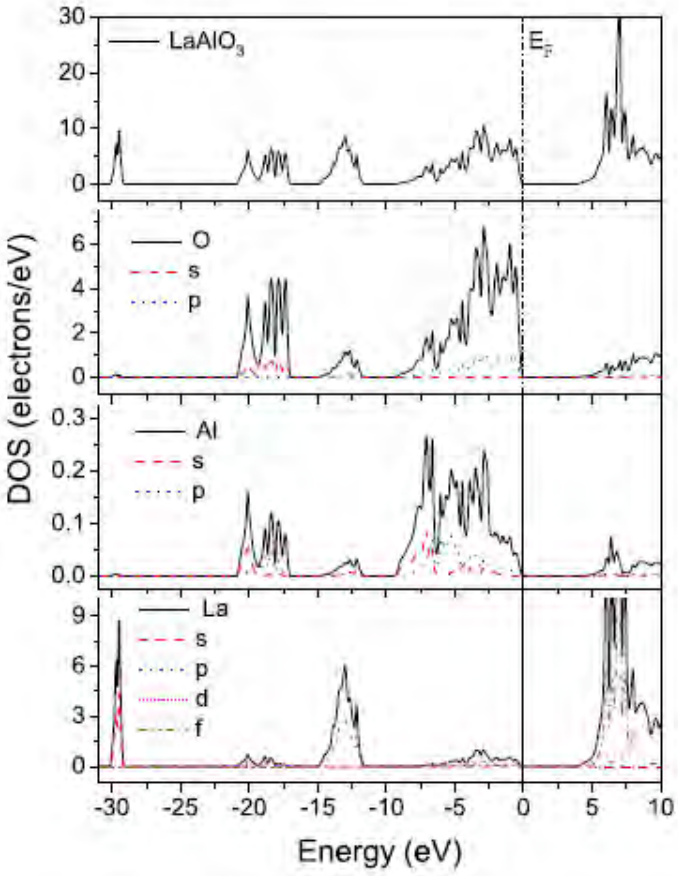

Figure 1.14: on-site angular momenta-projected *l*-DOS of rhombohedral LaAlO3 computed by [21]

The band structure and *l*-DOS in Figure 1.13 and 1.14 were performed by [21] using the density functional theory (DFT) with full-potential linearized augmented plane wave (FP-LAPW).

Similar to what we did for $SrTiO_3$, it is possible to study these 2 diagrams together to assign the bands. For the valence bands, the top of the valence bands from -9 to 0eV can be seen to be mainly made up of O 2p states with a mixture of Al sp and La p states. The O and Al sp are strongly mixed revealing a Al-O hybridization. On the other hand, the bottom of the conduction band (3.95-10eV) consists on mainly La 5d with La 4f states condensed in the region 6.2-7.2eV.

1.13. Graphene

Graphene has been extensively studied over the past decade after its discovery. It possesses great potential in the field of optics and electronics due to its intrinsic novel

properties. However, being a 2D material of monolayer thickness, it cannot be used on its own in electronic components. Instead, it requires some sort of a substrate onto which it can be placed. This hence places great emphasis on the interaction which goes on at the interface as it can heavily affect the properties of graphene.

Graphene is a 2D allotrope of carbon, where carbon atoms are located in a honeycomb lattice structure. The carbon atoms are sp^2 hybridized from the mixing of the one 2s and $2p_x$ and $2p_y$ orbitals. This forms a trigonal planar structure (120^o) centered about each carbon atom. The σ bond between the adjacent sp^2 orbitals lies in plane between each carbon atom with a distance of $a = 1.42\text{Å}$. The one electron per carbon atom left resides in the $2p_z$ orbital which is perpendicular to the plane and may bind covalently with neighboring atoms to form π bands. The lattice vectors and reciprocal lattice vectors of the graphene crystal structure are given in Eq. (3.1) and (3.2). [23]

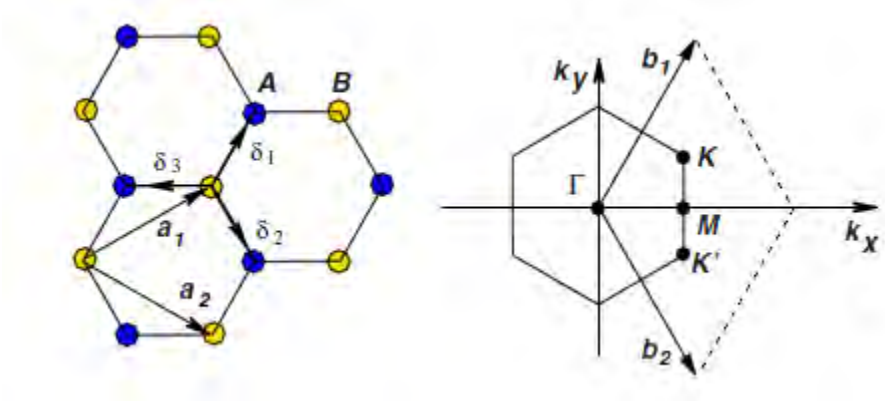

Figure 1.15a and b: Crystal lattice structure of graphene (left) and its Brillouin zone(right) [23]

$$\overline{a_1} = \frac{a}{2}(3, \sqrt{3}), \qquad \overline{a_2} = \frac{a}{2}(3, -\sqrt{3}) \tag{1.74}$$

$$\overline{b_1} = \frac{2\pi}{3a}(1, \sqrt{3}), \qquad \overline{b_2} = \frac{2\pi}{3a}(1, -\sqrt{3}) \tag{1.75}$$

1.13.1. Band structure of Graphene

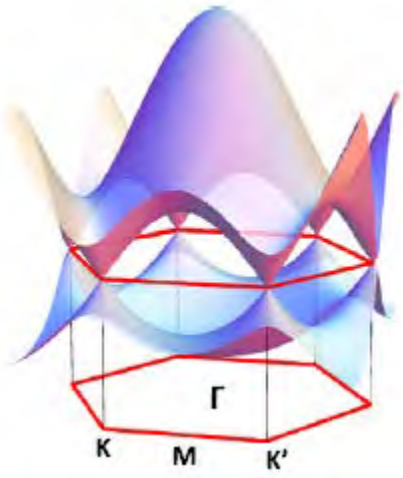

Figure 1.16: Energy dispersion of π bands in the graphene BZ [26]

By solving the tight-binding Hamiltonian for electrons in graphene, it is possible to derive the energy dispersion giving Figure 1.16.

$$E_{\pm}(k) = \pm t\sqrt{3 + f(k)} - t'f(k),$$
$$f(k) = 2\cos\left(\sqrt{3}k_y a\right) + 4\cos\left(\frac{\sqrt{3}}{2}k_y a\right)\cos\left(\frac{3}{2}k_x a\right) \quad (1.76)$$

Where t and t' are the nearest-neighbor and next nearest-neighbor hopping energy respectively. [23]

Near the K/K' point of the Brillouin zone, the band structure resembles a Dirac cone. At this point, the valence and conduction bands become degenerate and display a linear dispersion. Near this point, electrons start to behave as massless Dirac fermions with a velocity of about 10^8 cm/s as first shown by Wallace. [24,25]

Another peculiar point in the band structure is the M point where there exists a saddle point singularity. Typically, the region KM of the Brillouin zone is where low energy optical experiments such as our ellipsometry experiment (0.5-6.3eV) is of particular interest as it is not possible to excite electrons at the Γ point (band gap of about 20eV [27]) with this low range of energy.

1.13.2. Optical absorption in Graphene

The electronic properties of solids are largely related to their optical constants. Optical absorption, for instance, comes about from intraband and interband transitions.

In Graphene, intraband transitions dominate in the far-infrared region. [28] The intraband transitions are mainly due to free-carrier excitations and can be well described by the Drude model elaborated in Section 1.8.3. In the mid-infrared to near-infrared region, interband transitions start to dominate over intraband transitions. The response in this region is also found to be largely frequency independent and is approximated to a universal value defined by the fine structure constant. [26,29] In the UV range, interband transitions (near the M point) increases beyond this universal value and starts to display excitonic structures

Figure 1.17: Schematic diagram of intraband excitation near the Dirac point [26]

Intraband transitions are the excitation of electrons in the same band across the Fermi level. In Figure 1.17, we see a typical intraband transition in hole-doped graphene near the Dirac point. As we can see, due to the energy dispersion, the momentum of the electron is changed as well. However, in graphene, c/v_F~300 and the photon momentum hence is insignificant. To conserve momentum in such excitations, the electrons hence need to be scattered by phonons (which are temperature dependent) or defects. [26]

The Drude model describes intraband transitions based on the frequency dependent sheet conductivity

$$\sigma(\omega) = \frac{\sigma_0}{1 + i\omega\tau} \qquad (1.77)$$

where σ_0 is the dc conductivity. For massless Dirac fermions, the Drude weight, which is the integrated oscillator strength, is given by $D = e^2 v_F \sqrt{\pi n}$. [26,30]

Interband transitions on the other hand are excitations of electrons from the valence band to the conduction band via photon absorption. These transitions are presented as the blue arrows in Figure 1.18.

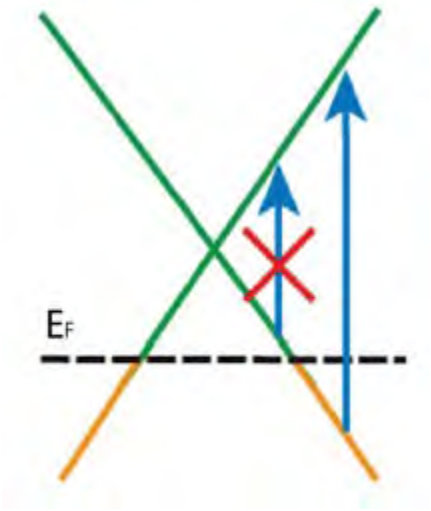

Figure 1.18: Schematic diagram of interband excitation near the Dirac point for hole-doped Graphene [26]

Under the tight-binding model, it is possible to calculate the optical sheet conductivity from interband transitions to give Eq. (1.78) below. [26,30]

$$\sigma_1(\omega) = \frac{\pi e^2}{4h}\left[\left(\tanh\frac{\hbar\omega + 2\epsilon_F}{4k_BT}\right) + \left(\tanh\frac{\hbar\omega - 2\epsilon_F}{4k_BT}\right)\right] \qquad (1.78)$$

Where ϵ_F is the Fermi energy and is assumed to be close to the chemical potential. It is easy to see in Eq. (1.78) that transitions with energy up to $2|\epsilon_F|$ are forbidden due to the doping as seen in Figure 1.18.

For T=0K, we see that the optical sheet conductivity in Eq. (1.78) then reduces to universal frequency independent constant given by $\sigma_1(\omega) = \frac{\pi e^2}{2h}$.

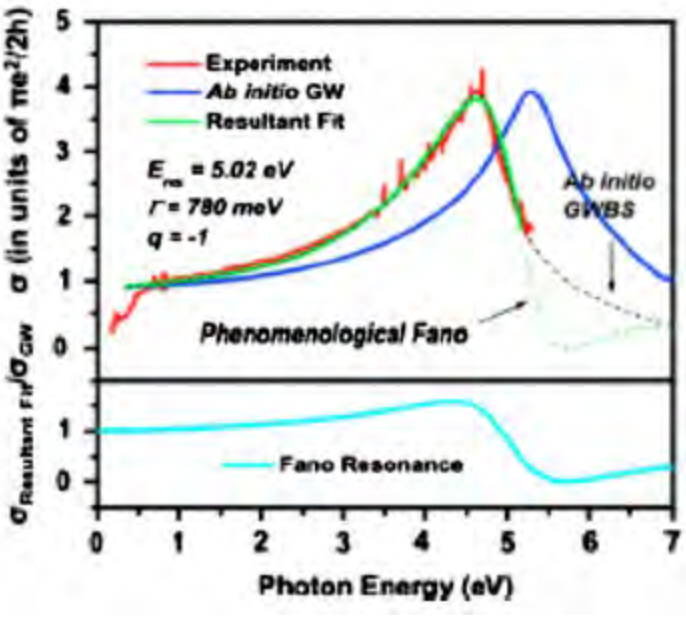

Figure 1.19: Excitonic effects on the optical response of Graphene [31]

Beyond the mid-infrared to near-infrared region, *ab-initio* GW calculations which take into account the band to band transitions and electron-electron interactions predict a symmetric peak near the M-point at 5.20eV [31] The GW calculations for graphene is shown in blue in Figure 1.18. The symmetry of the peak is due to the joint density of state (JDOS) being proportional to $-\log|1-(\omega/\omega_0)|$ for a 2D saddle point. [26]

The inclusion of electron-electron interaction in GW is essential as the Density functional theory local density approximation (DFT-LDA) calculation for a band structure underestimates the band gap of a solid. This is also known as the Kohn-Sham gap problem. By introducing electron-electron interaction in GW, we hence widen the band gap by shifting the absorption peak energy to a higher energy value. This is illustrated in Figure 1.19 where we see the GW calculations by [16] indeed opens up the band gap of graphene.

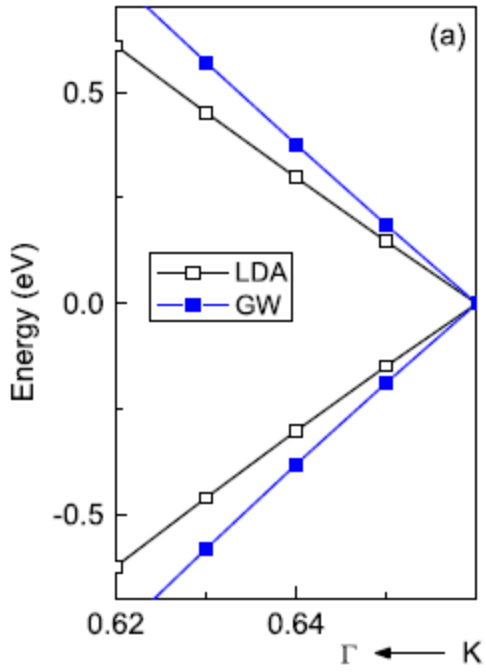

Figure 1.20: GW and LDA calculations near the Dirac point for graphene [16]

On the other hand, the Bethe-Salpeter equation (BSE) which takes into account electron-hole interaction by dealing with a two particle (electron-hole) correlation function, predicts an asymmetric peak at 4.6eV as shown in the black dotted line.

As shown in Figure 1.19, the GW-BSE correctly identifies the reflectivity experimental absorption spectra with the correct saddle point energy. [26] This correction shows that excitonic effects are important in graphene. The excitonic effects in graphene are however not due to bound excitons as described in Section 1.10 as graphene does not have a band gap but due to a redistribution of optical transition strengths by strong resonant excitons. [16]. This is essentially what the Fano resonance theory is about. The discrete excitonic states that lie below an continuous spectrum mixes with the continuum states to give an asymmetry transformation in the optical transition strengths near the saddle point singularity, a phenomenon known as *autoionization*. [13,17]

To understand further the Fano resonance, we may apply Fano line-shape analysis to the optical conductivity curves by [7,16,26]

$$\frac{\sigma(\omega)}{\sigma_{GW}\omega)} = \frac{(q+\varepsilon)^2}{1+\varepsilon^2} \qquad (1.79)$$

Where $\sigma_{GW}(\omega)$ is the GW sheet conductivity (without excitonic effects) and $\varepsilon = (\omega - \omega_{res})/ (\frac{\Gamma}{2})$ where ω_{res} is the resonance energy normalized by the width Γ, and q^2 denotes the ratio of the strength of the electron-hole interaction to the band to band transitions and the sign of q determines the asymmetry of the line shape.

As seen in Figure 1.19, the Fano fitting in green gives a good description of the experimental spectrum and is very close to the GW-BSE calculations. The GW-BSE spectrum is slightly broader by 200meV due to the rapid decay of the resonant excitons which are not included in the Fano line shape analysis. [26]

1.14. Motivation of this thesis

In this thesis, we aim to study the substrate effects of $SrTiO_3$ and $LaAlO_3$ for graphene. It is known that the substrate onto which graphene is placed on can have effects on the many body interactions at the interface. In the 2 extreme cases, it was found that in graphene on quartz (GOQ) interfaces, the electron-electron and electron-hole interaction was found to dominate with similar results to free standing graphene. [32] This shows that there is a weak interaction between graphene and quartz. However, the electron-hole interaction was found to be screened in graphene on copper (GOC) interfaces due to the electron doping as charge is transferred from the copper substrate to graphene. [32] We hence aim to extend the similar studies of the many body effects and the interplay of the electron-electron and electron-hole interactions in G/$SrTiO_3$ and G/$LaAlO_3$ interfaces.

Chapter Two: Experimental set-up and Simulations

In this chapter, we first begin by presenting the set-up of ellipsometer used in our experiment. Subsequently, we will be justifying the usage of ellipsometry as the choice of tool in our research using simulations. Ellipsometry, as discussed in Chapter One, is capable of thin film characterization, but it would be useful to compare ellipsometry with other thin film characterization methods to allow us to see the advantages of ellipsometry over the others.

To begin so, we will start by comparing the use of ellipsometry against reflectometry their effectiveness as well as accuracy in computing the dielectric function of a bulk substrate through a series of simulations.

2.1. Experimental Set-up

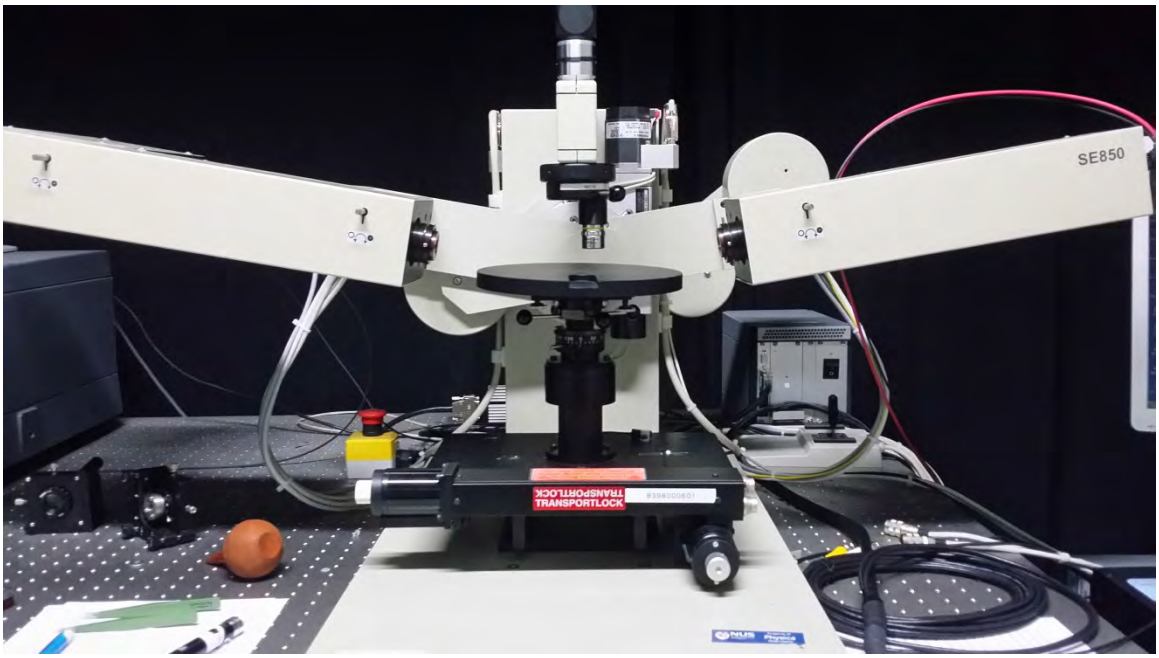

Figure 2.1: Actual SE850 ellipsometer in our lab

For this project, the spectroscopic ellipsometer SE850 is used to perform our experiment. The multi-chromatic light source is provided from 3 different light sources: near infrared source 0.5-1.5eV, UV-visible light 1.5-4.8eV and Deep UV 4.8-6.3eV to give us the broad experimental spectral range of 0.5-6.3eV.

The ellipsometry is performed in the RAE mode to help us extract the output polarization and a compensator is used at the incident end to increase the accuracy of measurement when $\Delta \approx 0^o$ or 180^o where the RAE mode alone shows inaccuracy. This is because the use of the compensator in the RAE mode allows the measurement of the extra Stokes parameter S_3 otherwise not possible. [1] The technical details are not shown explicitly.

The experiment is performed at room temperature in a non-vacuum environment and the samples used in our experiment are bought from Graphene Square Inc.

Raman Spectroscopy has been performed on the samples to ensure that there is only a monolayer thin film (Graphene) as well as being mostly defect free.

2.2. Reflectometry: Determination of bulk dielectric function

Reflectometry is an optical experiment very similar to ellipsometry with the exception that we are now wholly interested in the reflection coefficients, disregarding the phase change upon the reflection of light.

To simplify the experimental simulation calculation, we will be performing the reflectometry at normal incidence. However, this simple assumption here already starts to present a huge flaw in the sense that it is very difficult or impossible to perform such a normal incidence reflectometry experiment. This is because the optical path of the light source and the reflected light will lie on the same path. This hence produces an experimental set up difficulty of having the photodetector being blocked or blocking the light source, vice versa. To avoid this experimental set up difficulty, it is possible to perform the reflectometry in a near-normal incidence angle although the experimental results will be subjected to a slight inaccuracy if we do not take into account this slight angle variation.

For this simulation, we will be performing reflectometry at normal incidence on a bulk substrate with a light source capable of producing energy 0-7eV. Consider Eq. (1.28), the r_s polarization then gives us

$$r = \frac{1-\sqrt{\varepsilon}}{1+\sqrt{\varepsilon}} = \frac{1-n+ik}{1+n-ik} = \sqrt{R}e^{i\theta} \quad (2.1)$$

Since θ_1 and θ_2 are both 0.

From a known reflection coefficient, it is not possible to directly use the Kramers-Kronig relation of Eq. (1.72) and (1.73) to compute the dielectric function because the real and imaginary parts of the dielectric function depend on an unknown phase θ of the reflection coefficient. To solve this, we thus need to do a simple manipulation to Eq. (2.1) first. By taking the logarithm on both sides,

$$\ln r(\omega) = \ln\sqrt{R(\omega)} + i\theta(\omega) \quad (2.2)$$

From here, it is easy to then relate both sides by the Hilbert transform and hence derive a new Kramers-Kronig relation for the reflection coefficient and its phase.

$$\theta(\omega) = -\frac{2\omega}{\pi} P \int_0^{\infty} \frac{\ln \sqrt{R(\omega)}}{x^2 - \omega^2} dx + \theta(0) \quad (2.3)$$

With Eq. (2.3), we will be able to obtain $\theta(\omega)$ since $R(\omega)$ will be experimentally available to us. By solving Eq. (2.1) for n and k in terms of R and θ,

$$n = \frac{1 - R}{1 + R + 2\sqrt{R}\cos\theta} \quad (2.4)$$

$$k = \frac{2\sqrt{R}\sin\theta}{1 + R + 2\sqrt{R}\cos\theta} \quad (2.5)$$

We can hence compute the dielectric function with our known $R(\omega)$ and $\theta(\omega)$ using Eq. (1.18) and (1.19).

2.1.1 Problems and limitations faced in the simulation

It should be noted here that Eq. (2.4) and (2.5) are solved for r_s polarization in the convention, $N = n - ik$. One of the mistakes we have made in this simulation was forgetting to take note of the convention being used and using the wrong formulas for n and k to compute for the dielectric function. Additionally, we have also been misled by several papers which did not specify the polarization for which their n and k were derived. It was only when we found conflicting formulas from different sources, did we decide to re-derive the equations relating n and k to R and θ and hence find out wherein lies our problems. As an example to this, for the r_p polarization under the same convention of $N = n - ik$ gives us

$$n = \frac{1 - R}{1 + R - 2\sqrt{R}\cos\theta} \quad (2.6)$$

$$k = \frac{-2\sqrt{R}\sin\theta}{1 + R - 2\sqrt{R}\cos\theta} \quad (2.7)$$

Another problem faced was the integration limits and principal value in Eq. (2.3). In Eq. (2.3) the integration limits is stated to be 0 to infinity for the frequency (or energy), as brought forward from the Hilbert transform. However, this is realistically impossible since we there is an experimental limitation to how much frequency (or energy) of light we can provide. This therefore leads to need for an assumption to be made for the reflectivity beyond the experimental accessible range. As we shall show later, it is important to take note of how important this assumption is, as any possible artefacts beyond the experimental accessible range is immediately covered once we make this assumption. The effects of this assumption shall be further discussed in the following section.

Initially, we tried simulating a Lorentzian function reflectivity curve. However, this led to many problems which we had to troubleshoot. The results of simulating with a Lorentzian function reflectivity curve gave us an absorption curve (and hence ε_2) which was negative at some regions. This was physically impossible, and we presumed the problem lied in the integration with regards to the principal value.

Several papers suggest using a slightly modified Kramers-Kronig relation which takes care of the principal value

$$\theta(\omega) = -\frac{\omega}{\pi}\int_0^\infty \frac{\ln R(x) - \ln R(\omega)}{x^2 - \omega^2}\,dx \qquad (2.8)$$

Or equivalently,

$$\theta(\omega) = -\frac{1}{2\pi}\int_0^\infty \frac{d}{dx}(\ln R(x)) \ln\left|\frac{x-\omega}{x+\omega}\right| dx \qquad (2.9)$$

However, even after the application of Eq. (2.8) and (2.9), we failed to correct the problem of getting negative absorption at certain energy values. It was only after studying in depth on the Hilbert transform, did we realize that that the shape of the reflectivity curve cannot take the shape of a Lorentzian. i.e. such a reflectivity curve is unphysical in the real world. By studying the reflectivity spectra of different materials, we then changed the function of our reflectivity curve to a more physical and realistic reflectivity curve.

2.1.2 Reflectivity simulation I

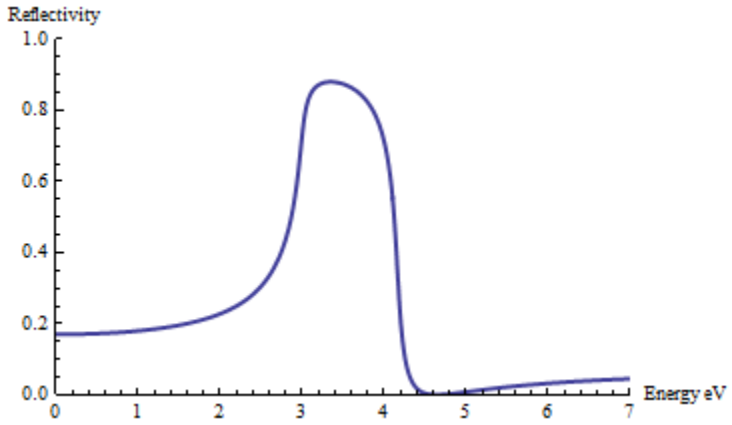

Figure 2.2: Simulated reflectivity spectra

In our first simulation, we have a reflectometer capable of performing reflectivity up to 7eV. To make use of the Kramers-Kronig relation, it is assumed that the reflectivity is a constant beyond 7eV.

Solving the integration in Mathematica, we found θ and hence computed n and k from Eq. (2.6) and (2.7).

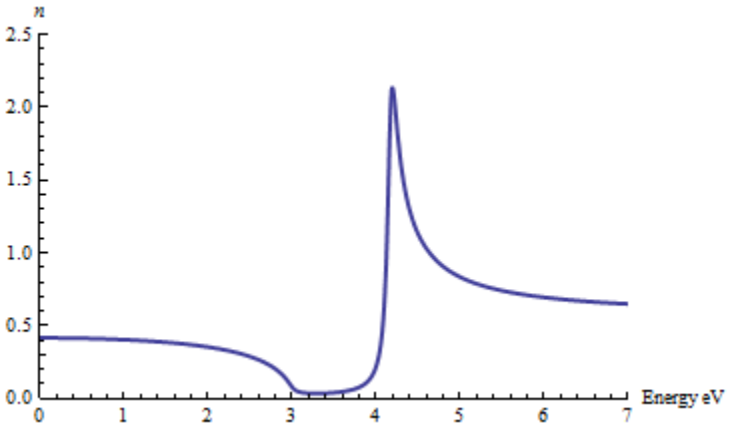

Figure 2.3: Simulated results for n, the refractive index

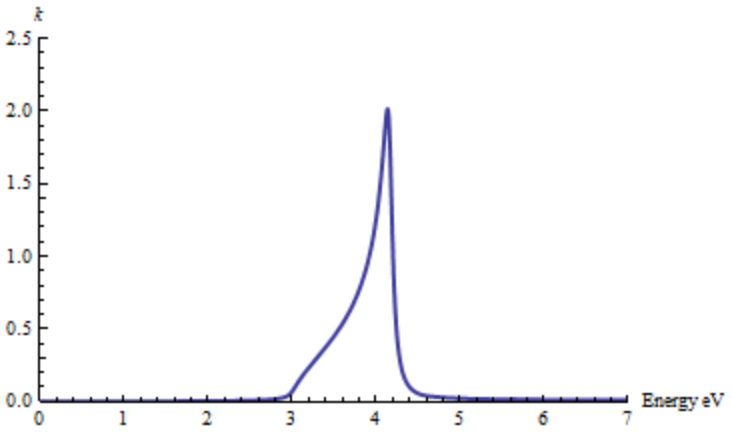

Figure 2.4: Simulated results for k, the extinction coefficient

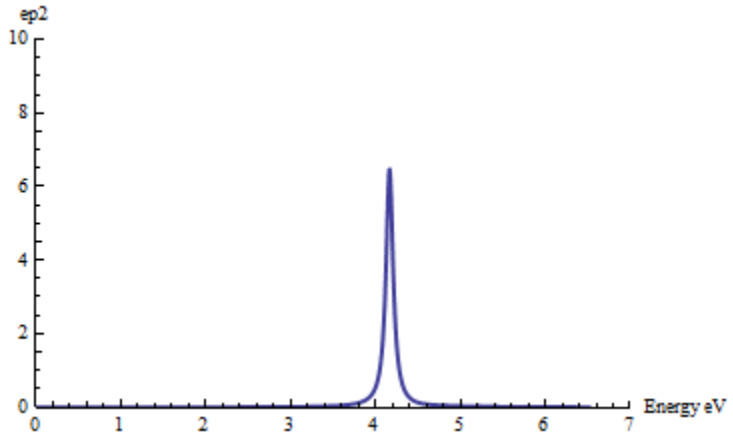

Figure 2.5: Simulated results for the imaginary dielectric function

2.1.3 Reflectivity simulation II

Using the same method as above to simulate for a 2nd reflectivity experiment, however, this time with a reflectometer capable of performing reflectivity up to 10eV. Suppose now that there was a secondary peak (artefact) which was covered up previously by our assumption.

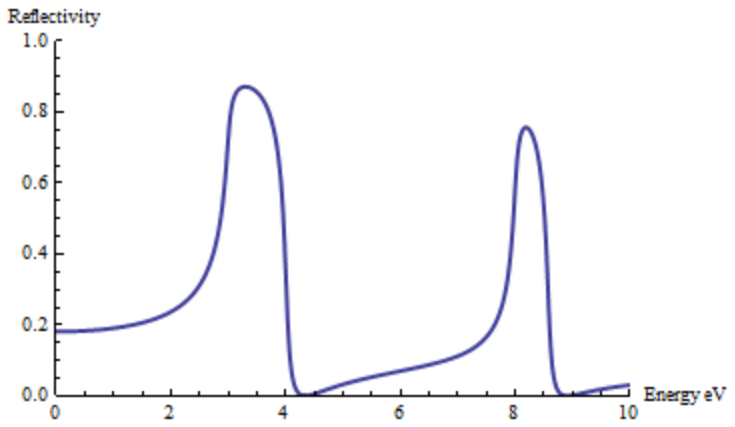

Figure 2.6: Simulated reflectivity spectra

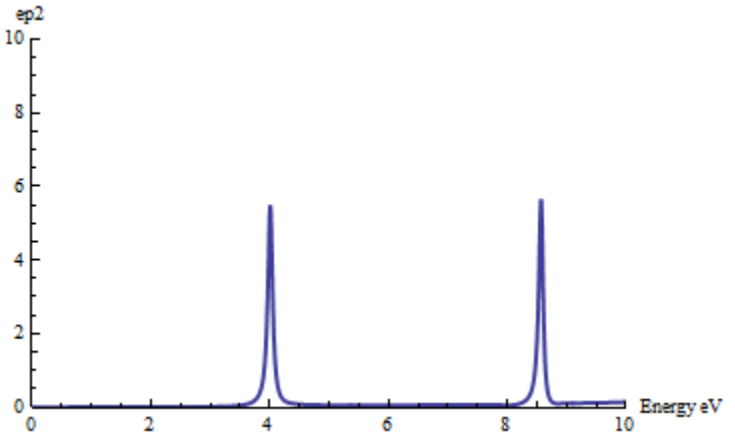

Figure 2.7: Simulated results for the imaginary dielectric function

2.1.4 Comparison between both reflectivity simulations

As seen in Figure 2.5 and 2.7 there are some difference between the imaginary dielectric peak at about 4eV. This difference worked out to be about 20%, which is a rather big discrepancy. This discrepancy proves that the Kramers-Kronig relation can lead to a big discrepancy in the experimental results obtained if the experimental range is not wide enough, or if an inappropriate assumption is made. In this case, the assumption made in Simulation I covered the secondary peak at 9eV which causes the integration in the Kramers-Kronig to be inaccurate.

2.3. Ellipsometry: Determination of bulk dielectric function

For a smooth bulk substrate, it is possible to write the experimental results of (ψ,Δ) directly into the dielectric function. Such a dielectric function is considered the pseudo-dielectric function, $\langle\varepsilon\rangle$.

For a simple 01 system, we may use Eq. (1.24) and (1.28) to show

$$\rho = \frac{r_p}{r_s} = \frac{\sin^2\theta_i - \cos\theta_i \left(\frac{\varepsilon_t}{\varepsilon_i} - \sin^2\theta_i\right)^{1/2}}{\sin^2\theta_i + \cos\theta_i \left(\frac{\varepsilon_t}{\varepsilon_i} - \sin^2\theta_i\right)^{1/2}} \tag{2.10}$$

By letting $\varepsilon_i = 1$ as in vacuum and $\varepsilon_t = \langle\varepsilon\rangle$, we can obtain

$$\langle\varepsilon\rangle = \sin^2\theta_i \left(1 + \tan^2\theta_i \left(\frac{1-\rho}{1+\rho}\right)^2\right) \tag{2.11}$$

Evidently, it can be seen from here that once the (ψ,Δ) are known for a particular energy range, the pseudo-dielectric function of the bulk substrate is immediately known. Additionally, the results gotten from the pseudo-dielectric function is independent of the experimental range unlike in reflectometry and does not require any kind of extrapolation of results.

It should be sufficient to see from Eq. (2.11) that the ellipsometry has clear advantages over reflectometry in the determination of the bulk substrate dielectric function. Although extending the experiments on multi-layered systems such as a thin film on bulk substrate, it becomes impossible to write the dielectric function in terms of the experimental parameters (ψ,Δ) directly, the disadvantages and inaccuracy of reflectivity still remains. Hence, although in a multi-layered system experiment, ellipsometry requires an indirect way of extracting the dielectric function from (ψ,Δ) , the final results still remain highly accurate.

Chapter Three: Experimental Results and Discussion

In this section, we bring the experimental results of our samples using ellipsometry. (Energy range 0.5-6.3eV) The samples being used in our experiment are Strontium Titanate ($SrTiO_3$) and Lanthanum Aluminate ($LaAlO_3$) as substrates for Graphene. The sample dimensions for both $SrTiO_3$ and $LaAlO_3$ are 10 mm X 10 mm X 0.5 mm as the substrate with a monolayer film of graphene of 3.3Å thickness. As discussed in the earlier sections, ellipsometry is performed on the bulk substrate first followed by on the monolayer graphene on the respective substrate. 4 different sections in this chapter bring us the results obtained for bulk $SrTiO_3$, bulk $LaAlO_3$, G/$SrTiO_3$ and G/$SrTiO_3$ respectively. All experiments are done at room temperature in a non-vacuum environment as mentioned in Chapter 2.

3.1. Optical spectra of $SrTiO_3$ (Results and Discussion)

As mentioned in earlier chapters, ellipsometry gives us the response of reflected light through 2 parameters, (ψ,Δ). And for the determination of a smooth bulk substrate, we may use Eq. (2.11) to compute the pseudo-dielectric function directly from our experimental data.

Although the pseudo-dielectric function can be computed using Eq. (2.11), to extract the dielectric function of a multi-layered system such as Graphene on $SrTiO_3$, we will need the Drude-Lorentz dielectric model of our bulk $SrTiO_3$ first as a supplement. We used a graphical program called Reffit to help us fit our experimental data and extract the Drude-Lorentz dielectric model of our bulk $SrTiO_3$ data.

Although there are many programs capable of fitting ellipsometry data, Reffit gives us the freedom of playing with the parameters in the Drude-Lorentz model and allow us to see physically how each parameter changes the output of our spectra.

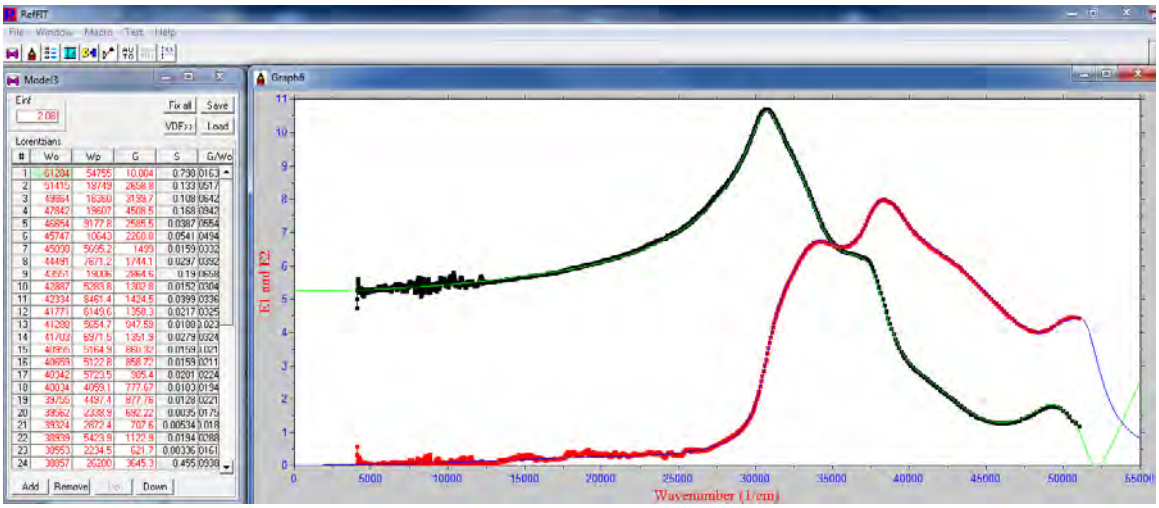

Figure 3.1: Screenshot of Reffit program in the dielectric fitting of bulk SrTiO3 ($\varepsilon_1, \varepsilon_2$)

Although not shown in full in Figure 3.1, a total of 46 oscillators were required for this fitting of bulk $SrTiO_3$.

In this section, we will also be using 2 sets of calculations from [6] to help us compare with our experimental results. These 2 sets of calculations are done in the RPA+GW and BSE+GW in the Tamm-Dancoff approximation.

In the computation of the absorption spectrum, it is important to consider many-body perturbation theory (MBPT) as the independent picture (IP) does not take into account essential responses in the medium such as screening effects or electron-hole interactions (such as a bound or continuum exciton). These effects can heavily change the optical spectra of a material and are hence of particular importance to absorption experiments such as ellipsometry. [6,13] Typically, the many-body exchange and correlation effects can be described by a nonlocal, non-Hermitian, and energy-dependent operator called the self-energy $\sum = iGW$. Where G is the one-particle Green's function and W is the screen coulomb interaction. [6]

The GW calculation takes into account band to band and electron-electron interaction. The Random Phase Approximation (RPA) accounts for the weakly screen coulomb interaction by assuming that the potential experienced by an electron is composed of 2 components, an external potential and potential from the induced charge density. [14,15] On the other hand, the Bethe-Salpeter equation (BSE) takes into account electron-hole interaction by dealing with a two particle (electron-hole) correlation function. [6]

In Figure 3.8, we compare the *ab initio* calculations from [6] with our experimental results. The results shown in Figure 3.2 for the RPA+GW and BSE+GW clearly show that by accounting for the electron-hole interaction, the structures are red-shifted and show an increase in amplitude.

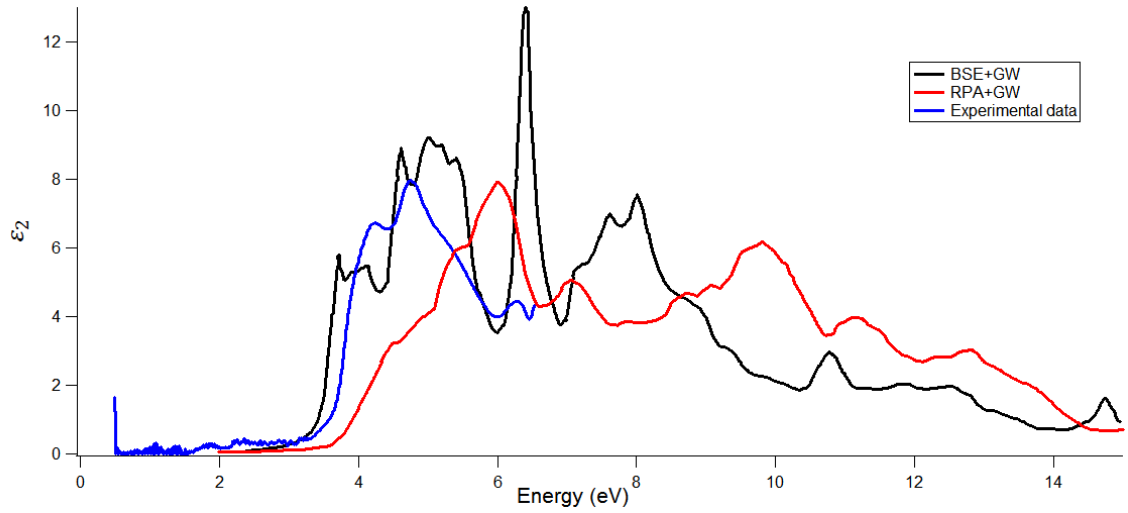

Figure 3.2: Absorption spectrum of SrTiO3computed by [6] compared to our ellipsometric data of bulk SrTiO3

From Figure 3.2, we see that the BSE+GW calculation gives a good description of the onset of our experimental absorption spectrum. Moreover, the peak structure positions at 5eV and 6.2eV are well reproduced coinciding with our experimental data although the intensity is strongly overestimated.

In comparison, RPA+GW reproduces the amplitudes of the structures in our experimental data well but the positions are blue-shifted by about 0.8eV due to the lack of excitonic effect consideration.

Although the overestimation of amplitude indicates that there is a too strong excitonic effect in the BSE+GW calculation, the corrected structure positions nevertheless verifies that excitonic effects are essential in the computation of the optical spectrum of SrTiO3. The amplitude of the peak can be damped by considering dynamical effects such as the frequency dependent W and electron-phonon coupling effects. [6]

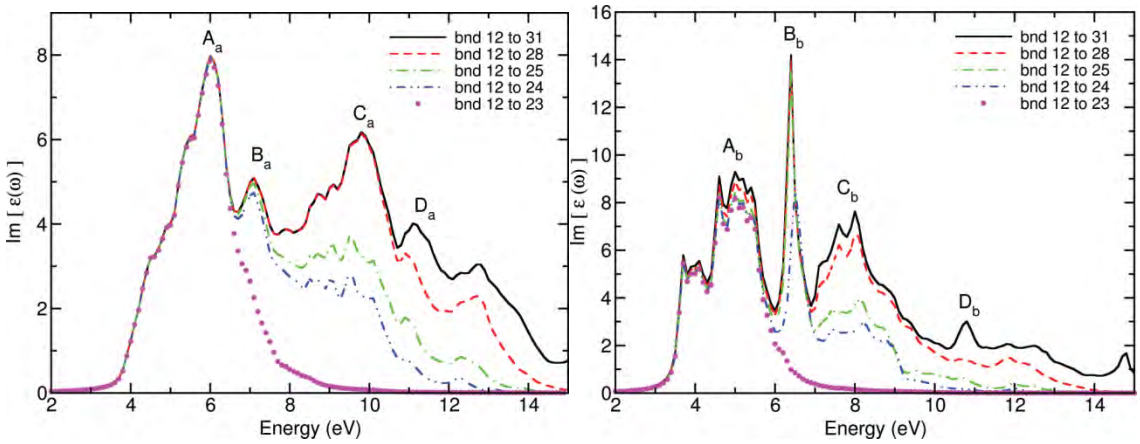

Figure 3.3a and b: RPA+GW(left) and BSE+GW(right) spectrum with the conduction bands included in the calculation progressively reduced to determine the roles each band play by [6]

To study the roles of which each bands play, a calculation was done progressively for each band to band transition by [6]. Based on Figure 3.3a and b, the structure A_a and A_b is due to transitions involving the Ti $3t_{2g}$ states (bands 21-23) only as they form almost the full spectra weight of the structure. As for structure B_a, based on Figure 3.3a, they are due to the transitions to Ti $3e_g$ states (bands 24,25) with band 24 making up 80% of the spectral weight. And likewise in Figure 3.3b, the structure B_b is made up of the Ti $3e_g$ states as well but each band now holds a 50% spectral weight. [6] Similarly, the transitions making up the structures of C and D can be determined in the same way but we will not be going into detail since they lie outside of the experimental range.

This analysis demonstrates that bands 24 and 25 from the Ti $3e_g$ states play a big role in the formation of the excitonic peak in B. Since structure B_b shows a strong and narrow exciton, it should come from a localized state. [6] By referring to the band structure of SrTiO3 in Figure 1.11 once again, we notice that band 24 is relatively flat and non-dispersing in the ΓX direction. It is suggested in [6] that the structure B_b is hence formed by the transitions from bands 19 and 20 to 24 along the ΓX direction.

By inferring from the analytical data provided extensively from [6], we hence conclude that the first structure in our experimental data at about 4.8eV is due to the transitions to the Ti $3t_{2g}$ states (bands 21-23). For our second structure at 6.2eV, this is most likely due to transitions from bands 19 and 20 to 24 along the ΓX direction where they are less dispersing. The damped peaks as compared to the theoretical work of GW+BSE are due to dynamical effects such as the frequency dependent W and electron-phonon coupling effects which were not included in the calculation.

3.2. Optical spectra of $LaAlO_3$ (Results and Discussion)

Using Eq. (2.11) to once again compute the pseudo-dielectric function of $LaAlO_3$, we obtain the bold line dielectric function as shown in Figure 3.10. To facilitate the extraction of results for G/$LaAlO_3$, we used Reffit to fit the data of bulk $LaAlO_3$ as we did for SrTiO3. A total of 30 oscillators were used to fit the pseudo-dielectric function.

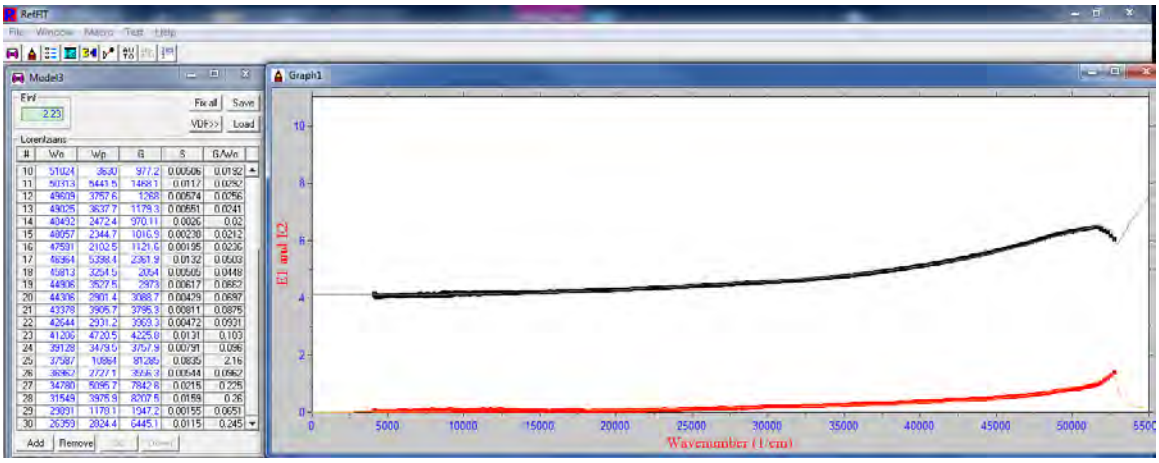

Figure 3.4: Screenshot of Reffit program in the dielectric fitting of bulk $LaAlO_3$

In Figure 3.5, we compare our experimental results of the imaginary dielectric function with theoretical results computed by [21] using FP-LAPW which revealed a 6.1eV optical band gap.

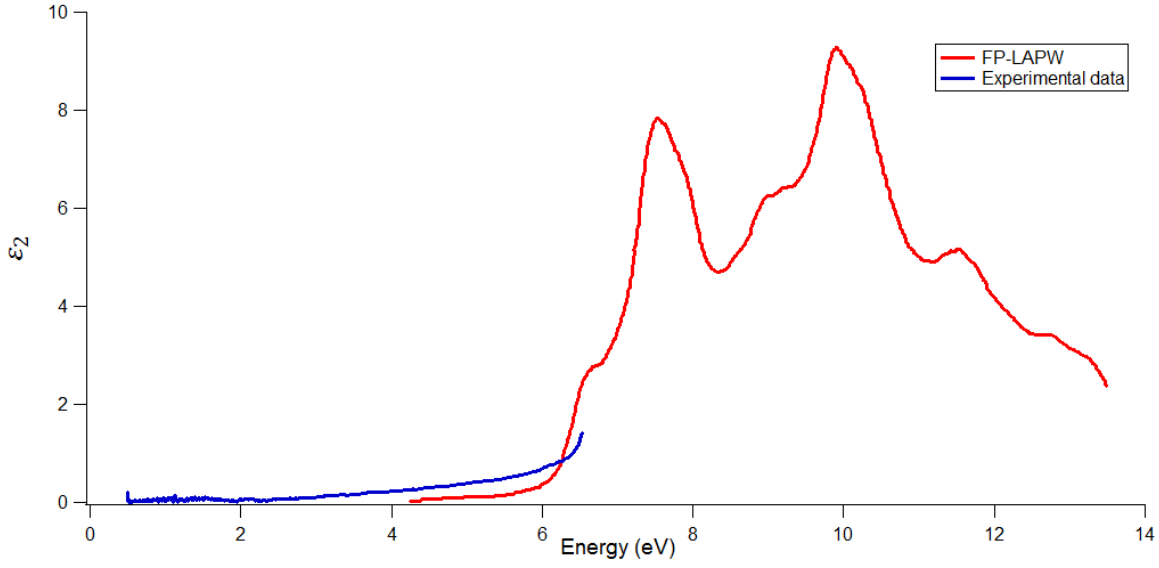

Figure 3.5: Absorption spectrum of $LaAlO_3$ computed by [21] compared to our ellipsometric data of bulk $LaAlO_3$

As shown in Figure 3.5, there is little to be discussed as the energy range of our experiment was too short. (up to 6.3eV) The calculation seem to describe well the absorption onset of our experimental data but due to the limitation of out experimental set up, we cannot study if the structures beyond 6.3eV were reproduced in our experimental data. Due to this experimental limitation, it is hence also not possible to extract the optical band gap of bulk $LaAlO_3$ from the experimental absorption spectrum.

By studying the *l*-DOS in Figure 1.14, we suggest that the absorption onset is most likely due to transitions from the O 2p to La 4f states.

3.3. G/SrTiO3 results and Discussion

The effects of graphene on $SrTiO_3$ can drastically change the experimental parameters of (ψ,Δ) as shown in Figure 3.6 below. Although the graphene is only of monolayer thickness, ellipsometry is able to detect the changes in the system regarding how the sample reacts to the incident light. This further demonstrates the sensitivity of ellipsometry to thin films and hence choice of research tool.

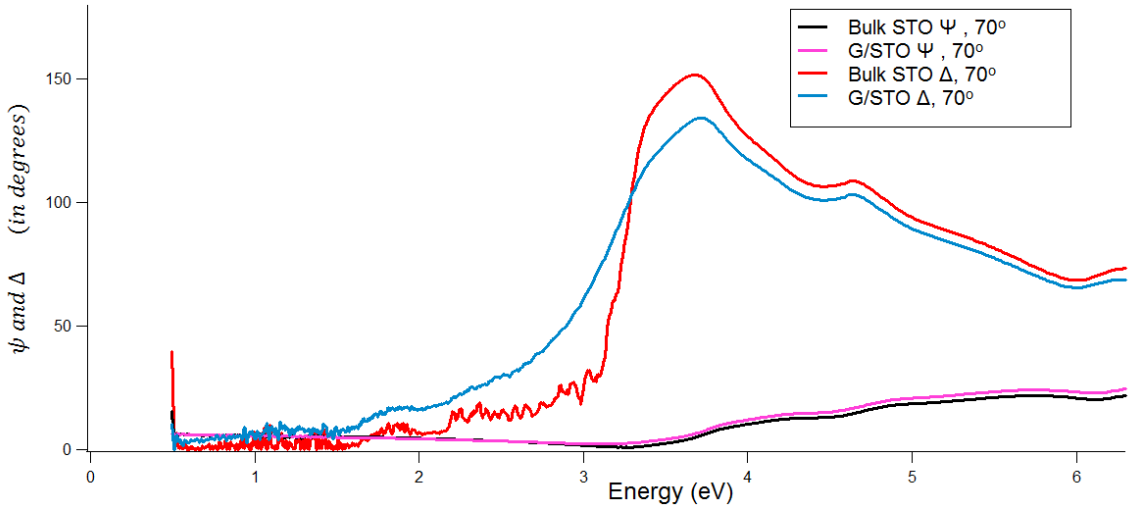

Figure 3.6: Experimental data of (ψ,Δ) for bulk SrTiO3 and G/ SrTiO3 system with incident angle 70°

For the fitting of a $G/SrTiO_3$ multilayered system, we used model -33 in Reffit to help us with the fitting. The details of the model used are omitted. The Drude-Lorentz model for the bulk substrate $SrTiO_3$ has already been obtained in Section 3.1, we played with the 2nd layer Drude-Lorentz dielectric model to obtain the computed (ψ,Δ) spectra fitting of the $G/SrTiO_3$ system. To increase the accuracy of our results, we used a simultaneous fitting of incident angles 50°, 60° and 70°. In Figure 3.7-3.9, we show the results of our

fittings for a monolayer graphene of 3.3Å. Raman spectroscopy has been used to verify that there is only a monolayer graphene hence we kept the thickness of graphene fixed at about 3.3Å. The mean squared errors (MSE) calculated for the 50^{o}, 60^{o} and 70^{o} spectra are 0.036, 0.038 are 0.058 respectively.

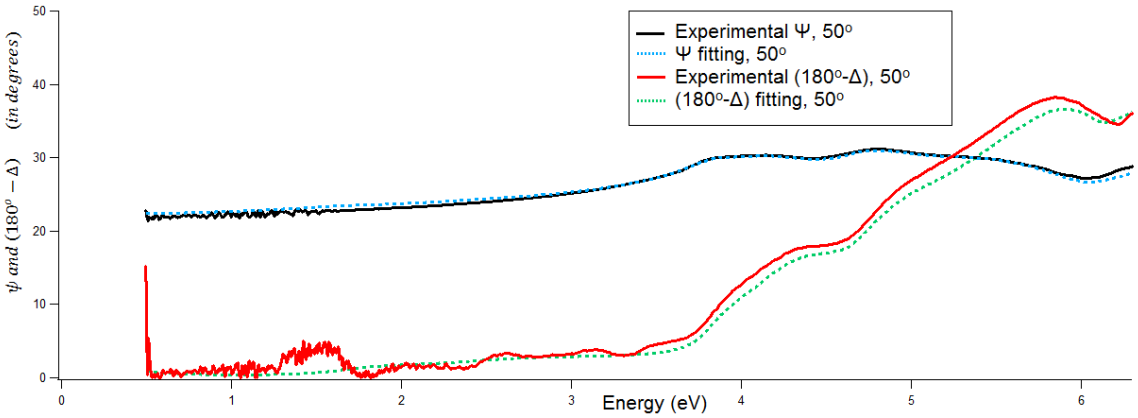

Figure 3.7: Simultaneous fitting of G/SrTiO3 (ψ,Δ) 50^{o}

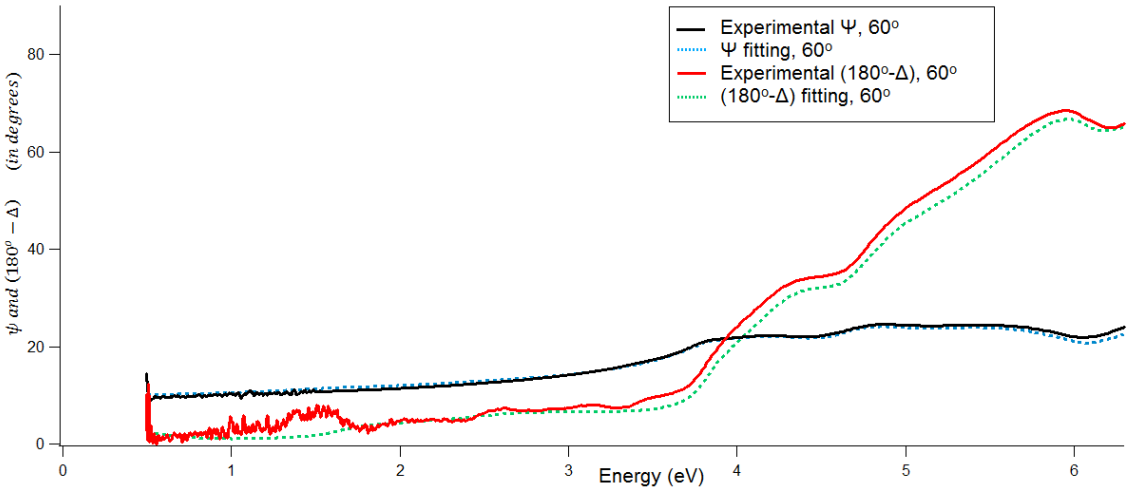

Figure 3.8: Simultaneous fitting of G/SrTiO3 (ψ,Δ) 60^{o}

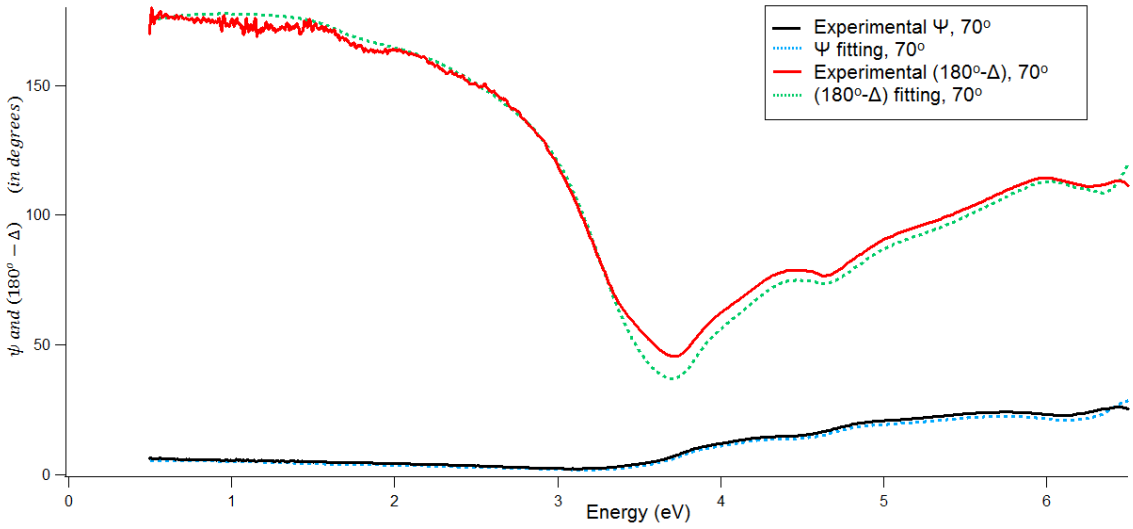

Figure 3.9: Simultaneous fitting of G/SrTiO3 (ψ,Δ) 70°

The simultaneous fitting of $G/SrTiO_3$ is considerably decent although there is some discrepancy in the Δ for all 3 incident angles after 3.3eV. This could be due to some imperfections in our sample since in our fitting we assumed that the optical model of $G/SrTiO_3$ to be perfectly smooth and free from impurities. In reality, this is hardly true for any sample. It is very difficult to fabricate a sample perfectly free from any adatoms or vacancies. Furthermore, as the experiment was done in a non-vacuum environment, it could be possible that some sort of impurity layer exists on the sample hence affecting our experimental data.

Technically, it is possible to model a roughness layer in the optical model of our sample to take into account of this. [1] However, the fitting program which we used, Reffit, does not have an approach to take into account of this roughness layer.

The results of our fitting certainly can be improved, but further studies on the sample's film structure needs to be performed first. One of the disadvantages of ellipsometry is that if the sample has too many unknowns it may become exponentially harder to find an accurate extraction of the dielectric function as the analytical parameters have too wide of a range. Supplementary characterization techniques such as scanning electron microscope (SEM), transmission electron microscope (TEM), and atomic force microscope (AFM) can be used to help us determine a more accurate film structure first so we can apply a roughness layer appropriately using another fitting program.

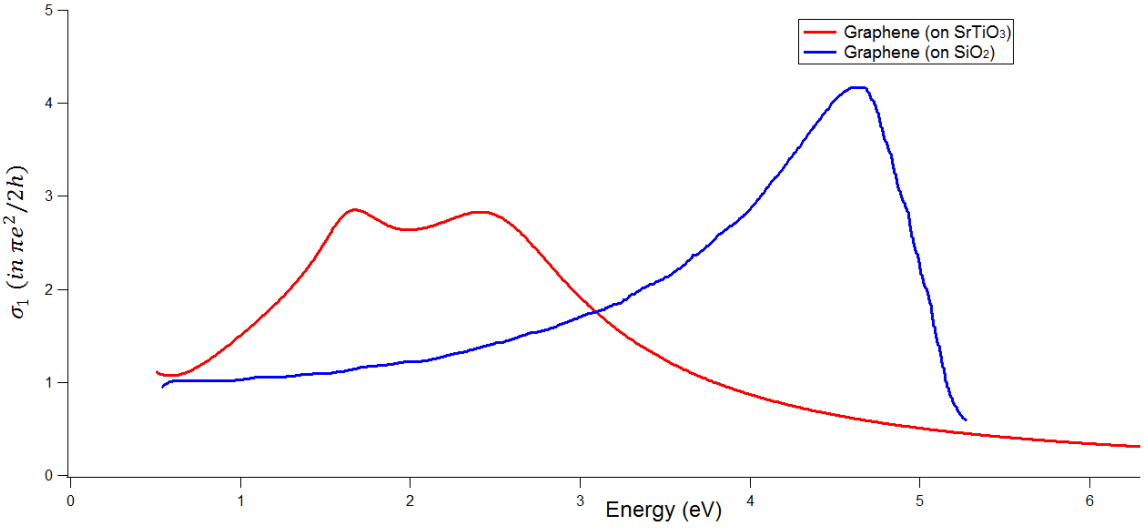

Figure 3.10: Extracted sheet conductivity of Graphene on SrTiO3 (red) compared to extracted conductivity of Graphene on SiO_2 (blue) from [33]

In Figure 3.10, we show the extracted sheet conductivity for the monolayer graphene on $SrTiO_3$ substrate. We compare our results in Figure 3.10 to the case of graphene (on SiO_2). To recap, in [31] the GW calculation shows a peak at 5.2eV and the GW-BSE calculation red-shifts this peak down to 4.6eV due to the consideration of e-h interaction. This peak corresponds to the Van Hove singularity at the M point of the BZ of graphene band structure. In the G/$SrTiO_3$ system however, there is large renormalization in the optical spectra with 2 peak structures of similar amplitude appearing at 1.7eV and 2.5eV. This suggests strong interaction at the interface between graphene and $SrTiO_3$ as the band structure of the graphene on the $SrTiO_3$ system has been altered.

To further analyze and give a more detailed explanation of the interaction at the interface, an *ab initio* calculation for the composite system would be required. Since our sample is Graphene on $SrTiO_3$ (001), there are possibilities of strong hybridizations between the C p_z orbital of graphene with O p_z, Sr d_z^2 and Ti d_z^2 orbitals, which a DFT calculated band structure and *l*-DOS spectra can probably shed light on as we had in Section 1.11.1 and 1.12.1 for the cases of bulk $SrTiO_3$ and $LaAlO_3$.

The red-shift and asymmetry of the optical spectra suggests e-h interaction present in the system and further investigation through the Fano line-shape analysis (Eq. 1.79) as described in Section 1.13.2 can be performed on the optical spectra. The parameters in Eq. 1.79 used to fit the optical spectra can shed light on the resonant exciton energy as well as its lifetime. Typically, this will also tell us the lifetime as it can be determined from the width of the peak based on Heisenberg's uncertainty principle.

Also, another key structure in the sheet conductivity obtained is that it demonstrates UV transparency after the 2nd peak at 2.5eV. We see that after this peak, the sheet conductivity quickly falls off in the UV range.

We see that $SrTiO_3$ indeed has strong interaction with graphene. The extracted graphene sheet conductivity no longer resembles the case of free standing graphene. The strong interaction, which we propose could be due to strong hybridizations between the bands, significantly changes the optical spectra of graphene, different from the case of Graphene on SiO_2/Si where it behaves more or less like a free standing graphene. i.e. negligible interaction. Some key features however, like the fall off the sheet conductivity to the universal value at the mid to near infrared region, remains unchanged.

3.4. G/$LaAlO_3$ results and Discussion

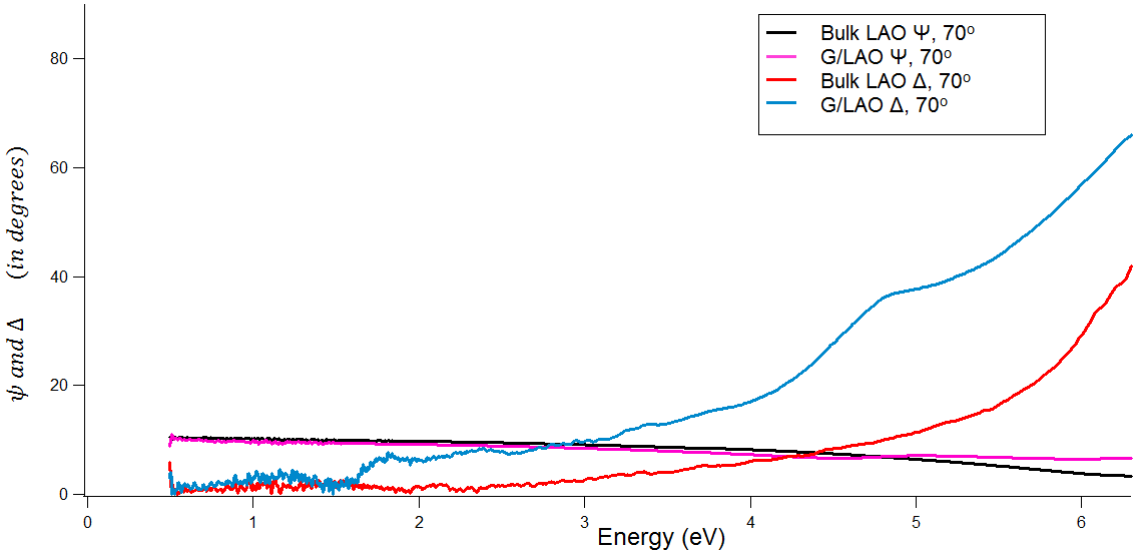

Figure 3.11: Experimental data of (ψ,Δ) for bulk $LaAlO_3$ and G/$LaAlO_3$ system with incident angle 70°

Here we see again considerable difference in the (ψ,Δ) spectra just after adding one monolayer of graphene. This once again showcases the sensitivity of ellipsometry.

Similar to what we did in Section 3.3 for the G/$SrTiO_3$ case, we show the results of our simultaneous fitting of 50°, 60° and 70° (ψ,Δ) spectra in Figure 3.12-3.14 below. The graphene film thickness is fixed at 3.3Å as well for G/$LaAlO_3$. A total of 23 oscillators were used in this fitting.

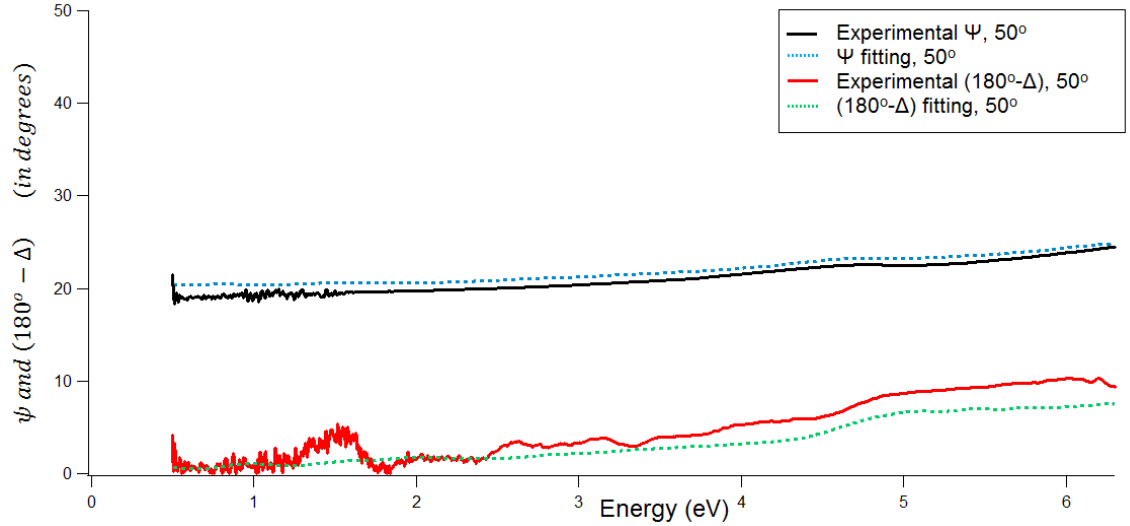

Figure 3.12: Simultaneous fitting of G/$LaAlO_3$ (ψ,Δ) 50°

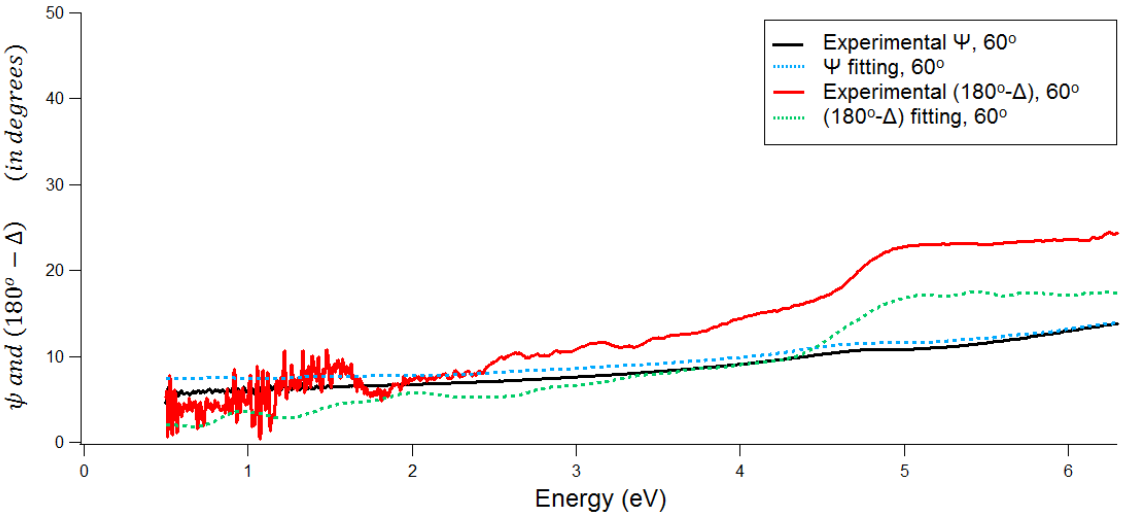

Figure 3.13: Simultaneous fitting of G/LaAlO$_3$ (ψ,Δ) 60°

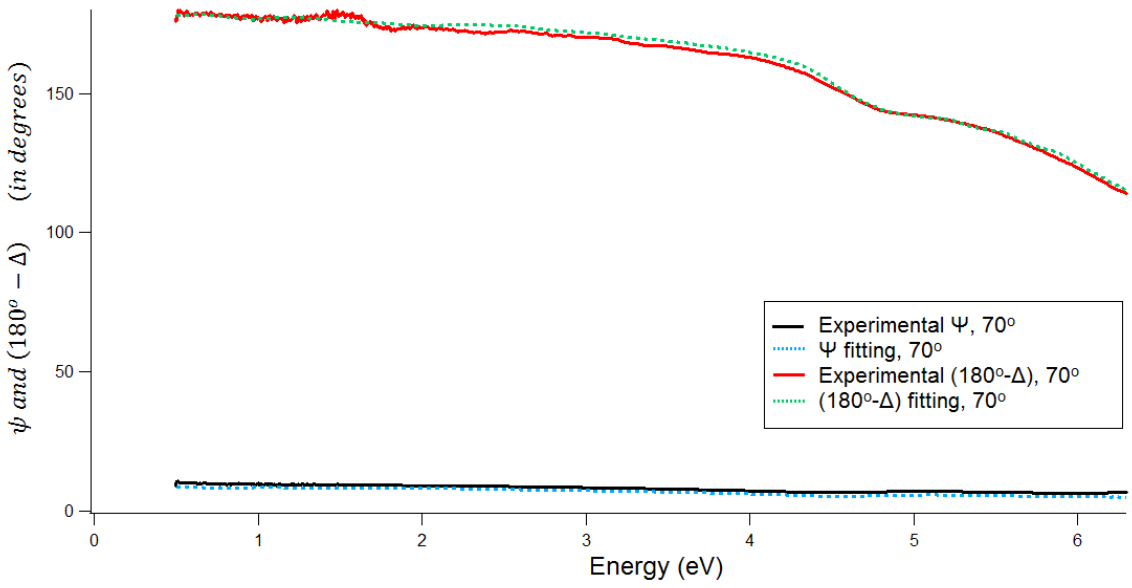

Figure 3.14: Simultaneous fitting of G/LaAlO$_3$ (ψ,Δ) 70°

To avoid any misleading of information, although it may look like the fitting for 50° and 60° to be much worse than the case of 70°, it should be highlighted here that the y-axis of the graphs are of different scale. The MSE for the 50°, 60° and 70° spectra are 0.11, 0.17 and 0.15 respectively.

As in the case of the G/$SrTiO_3$ in Section 3.3, similar techniques can be used to improve our fitting by using supplementary experiment information to build on our knowledge of the film structure and hence improve our optical model. In this case, it was almost impossible to lift our fitting of Δ in Figure 3.11 and 3.12 just by varying the parameters of our model as ascertained through trail and error. This leads to our deduction that the discrepancy hence must be due to some sort of roughness layer or impurities missing in our optical model. A similar improvement as in the case of G/$SrTiO_3$ to the fitting can be done by performing supplementary experiments to better understand the film structure first.

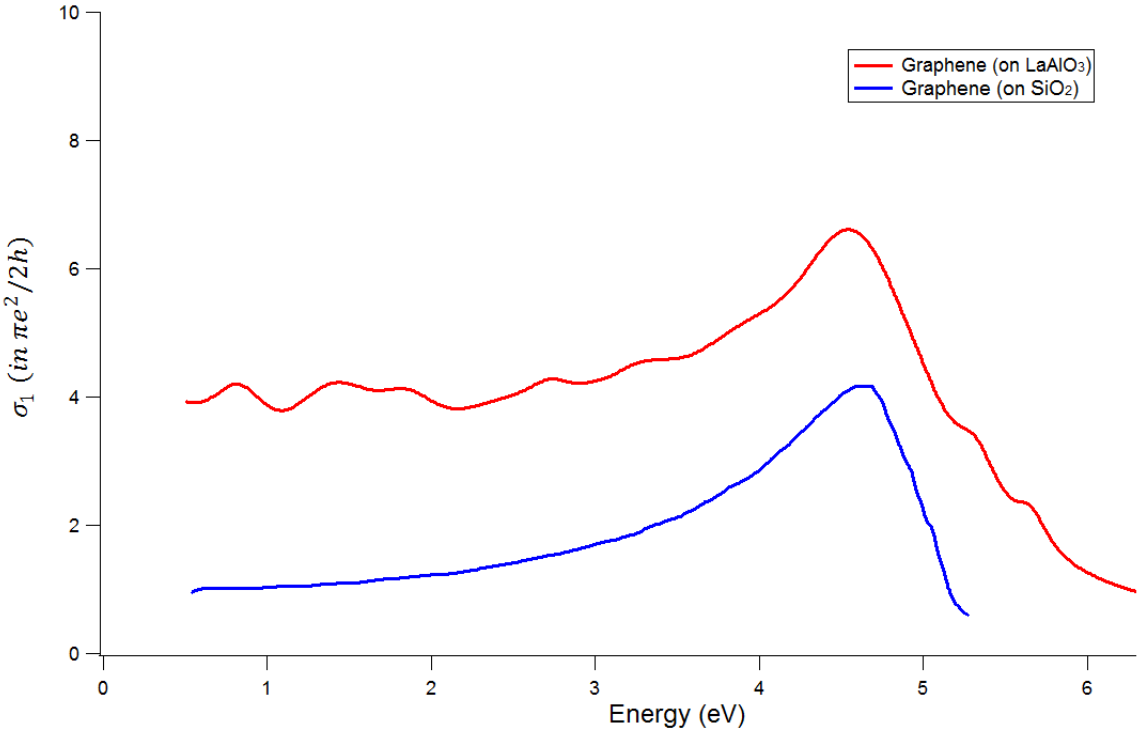

Figure 3.15: Extracted sheet conductivity of Graphene on $LaAlO_3$ (red) compared to extracted conductivity of Graphene on SiO_2 (blue) from [33]

In Figure 3.15, we present the sheet conductivity of graphene on $LaAlO_3$. As seen in Figure 3.15, the optical spectrum has changed significantly with respect to the case of graphene (on SiO_2/Si). Some characteristic features are unchanged though. We observe a peak structure at 4.6eV, similar to the case of graphene (on SiO_2/Si) as shown in blue. However, for the case of G/$LaAlO_3$, it was found that the optical conductivity does not

reduce to the universal value of $\pi e^2/2h$ in the IR region anymore. Instead, a relatively constant sheet conductivity of $4\pi e^2/2h$ was observed in the IR-visible region (0.5-3eV).

In the case of free standing graphene, the linear bands near the Dirac point (0.5-1.2eV) are the ones that give rise to this frequency independent universal conductivity. [26] Therefore, now for the case of G/$LaAlO_3$, the linear bands are expected to extend over a wider energy range (0.5-3eV). Secondly, since the amplitude of the frequency independence of sheet conductivity (and hence absorption) is higher in the G/$LaAlO_3$case, we expect that this linear dispersion to be less steep than the free standing graphene case since a less steep dispersion allows for more absorption of photons.

Also, we can expect that the Van Hove singularity at the M-point (4.6eV) to be the same in both cases since the peaks of both curves coincide. In both cases, this peak corresponds to the flat dispersion bands in the M-point. Since there is now a flat dispersion, more photons of the same energy can be excited and hence resulting in a peak in the optical spectrum.

However like before, it is hard to give an explanation why this would happen without any supplementary *ab initio* calculations. It will be interesting to see what kind of interaction actually occurs between graphene and $LaAlO_3$ in future work. The optical spectrum also shows hints of asymmetry, indicating the presence of resonant excitons which we will need Fano line-shape analysis to quantify.

We hence see that the interaction between Graphene and $LaAlO_3$ as a substrate is not as strong as in the case of Graphene on $SrTiO_3$ where we saw huge shifts and new peaks appearing. In this case, we saw that some characteristic features of free standing graphene still remains which could be due to their relatively larger band gap as compared to $SrTiO_3$.

3.5. Future work

As mentioned in Section 3.3 and 3.4, a lot of further study needs to be performed on the samples to give us a more accurate picture.

Firstly, on our part, improvements on the experimental results can be achieved. This can be done so by firstly taking a longer measurement in ellipsometry. If we notice the experimental data (for example Figure 3.13) in the IR region, it has very high noise due to the low intensity and hence high signal-to-noise ratio of IR photons. This noisiness can be reduced simply by taking a longer measurement. Also, we can improve the probability of impurities being present on the sample by performing the experiment in a vacuum environment.

Another point we have discussed is the addition of a roughness layer in our optical model to make the fitting more realistic. However, the addition of such a layer is not so trivial as it requires a better understanding of the film structure using supplementary experiments such as AFM.

Secondly, DFT band calculations and *l*-DOS of graphene on the composite systems can give us a more analytical picture and help us answer what kind of possible hybridization or charge transfer exist between the graphene and substrate bands there could be. As seen in the case of G/$SrTiO_3$ in Section 3.3, the considerable change in the optical spectra suggests that the band structure of the extracted graphene layer has changed significantly due to the strong interaction with the $SrTiO_3$ substrate.

Also, we are still missing the Fano line-shape analysis on Figure 3.10 and 3.15 for G/$SrTiO_3$ and G/$LaAlO_3$. Without the Fano line-shape analysis, it is hard to give a physical picture of how much the resonant excitons renormalize the graphene optical spectra to give it an asymmetric shape.

Finally, it will also be interesting to see the dependence of the sheet conductivity of our samples with regards to temperature variations. This will enlighten us on the changes in the Fano resonance occurring in our samples with respect to temperature, and any possibilities of controlling the resonant excitons for future applications might become clearer then. However, we can expect this to be very challenging as we will need to analyze the optical spectrum at each temperature individually first using the *ab initio* calculations to understand the interactions before we can put them together for comparison. Moreover, both $SrTiO_3$ and $LaAlO_3$ exhibit a phase transition (AFD) after a certain critical temperature which we must remember to take into account.

3.6. Conclusion

It can be seen clearly that the substrate of which graphene is placed on can hugely affect the optical spectra of graphene. This is due to a strong interaction between graphene and the substrate from possibly hybridizations or charge transfer effects. The results presented in Figure 3.3 and 3.4 clearly show that graphene can have large interactions depending on the substrate it is placed on. Typically, larger band gaps substrates such as SiO_2, and for our case $LaAlO_3$, seem to have lesser interaction with graphene as compared to $SrTiO_3$ as a substrate.

On the other hand, $SrTiO_3$ with a band gap of about (~3.2eV) perturbs the monolayer graphene more strongly in our experimental range. This suggests significant restructuring in the band structure of graphene on the $SrTiO_3$ substrate as we see new peak structures appearing and red shifts in the optical spectrum.

However, it is difficult to give a more analytical picture as for what kind of hybridization or coupling exists at the interfaces without supplementary data. Furthermore, the analysis of our optical spectra can be more detailed if we perform Fano line-shape analysis to give us insights on the Fano resonance present.

The depth of the work presented in this thesis can definitely be gone into more detail with more supplementary data; however, we should realize that this thesis has also opened the door to a wide breath of future development, of which includes the temperature dependence of the sheet conductivity of our samples.

References

[1] Fujiwara, H. (2007). Principles and Applications: Spectroscopic Ellipsometry. Maruzen Co. Ltd, Tokyo, Japan.

[2] Dresselhaus, M. S. (n.d.). SOLID STATE PHYSICS Part II: Optical Properties of Solids. MIT.

[3] Fox, M. (2001). Optical Properties of Solids. Oxford University Press.

[4] Kuzmenko, A. B. (2005). Kramers-Kronig constrained variational analysis of optical spectra. American Institute of Physics, Volume 76, Issue 8.

[5] Liu, Y.-W. (2012). Hilbert Transform and Applications, Fourier Transform Applications. Taiwan: InTech. Retrieved from InTech: http://www.intechopen.com/download/get/type/pdfs/id/36434

[6] Lorenzo Sponza, V. V. (2013). Role of localized electrons in electron-hole interaction: The case of SrTiO3. PHYSICAL REVIEW B.

[7] Elsasser, K. v. (2001). Bulk electronic structure of SrTiO3: Experiment and theory. JOURNAL OF APPLIED PHYSICS, VOLUME 90, NUMBER 12.

[8] Amar, F. G. (2011). *Atomic Orbitals*. Retrieved from Chemistry 121 : http://chemistry.umeche.maine.edu/~amar/spring2011/FG06_21.JPG

[9] Cavalab. (n.d.). *Solid State Chemistry Research Group*. Retrieved from Princeton University: https://www.princeton.edu/~cavalab/tutorials/public/structures/perovskites.htm

[10] van Heeringen, L. (2012). The band structure of SrTiO3/LaAlO3 heterostructures The k· p envelope function approach.

[11] A. Okazaki and M. Kawaminami. (1973) Lattice constant of strontium titanate at low temperatures. *Materials Research Bulletin*, Volume 8, No. 5

[12] L. F. Mattheiss. (1972) Energy bands for KNiF3, SrTiO3, KMoO3, and KTaO3, *Phys. Rev. B.* Volume 6.

[13] Gogoi, P. K., Santoso, I., Saha, S., Wang, S., Neto, A. H. C., Loh, K. P., ... & Rusydi, A. (2012). Optical conductivity study of screening of many-body effects in graphene interfaces. EPL (Europhysics Letters), 99(6), 67009.

[14] László Mihály, M. C. (2009). Solid State Physics. John Wiley & Sons.

[15] Neil W. Ashcroft, D. N. (1976). Solid state physics. Saunders College.

[16] Yang, L., Deslippe, J., Park, C. H., Cohen, M. L., & Louie, S. G. (2009). Excitonic effects on the optical response of graphene and bilayer graphene. *Physical review letters*, 103(18), 186802.

[17] Fano, U. (1961). Effects of configuration interaction on intensities and phase shifts. *Physical Review*, 124(6), 1866.

[18] del CastilloMussot, M., & Sham, L. J. (1985). Excitonic effect in the optical spectrum of semiconductors. Physical Review B, 31(4), 2092.

[19] A. Nakatsuka, O. Ohtaka, H. Arima, N. Nakayama, and T. Mizota. (2005) Cubic phase of single crystal $LaAlO_3$ perovskite synthesized at 4.5gpa and

1273K, *Acta Crystallographica Section E: Structure Reports Online*, vol. 61

[20] Hayward, S. A., Morrison, F. D., Redfern, S. A. T., Salje, E. K. H., Scott, J. F., Knight, K. S., ... & Carpenter, M. A. (2005). Transformation processes in La Al O 3: Neutron diffraction, dielectric, thermal, optical, and Raman studies. Physical Review B, 72(5), 054110.

[21] Luo, X., & Wang, B. (2008). First-principles study of the electronic and optical properties in rhombohedral LaAlO3. Journal of Applied Physics, 104(5), 053503.

[22] Howard, C. J., Kennedy, B. J., & Chakoumakos, B. C. (2000). Neutron powder diffraction study of rhombohedral rare-earth aluminates and the rhombohedral to cubic phase transition. Journal of Physics: Condensed Matter, 12(4), 349.

[23] Neto, A. C., Guinea, F., Peres, N. M. R., Novoselov, K. S., & Geim, A. K. (2009). The electronic properties of graphene. Reviews of modern physics, 81(1), 109.

[24] Zhang, Y., Tan, Y. W., Stormer, H. L., & Kim, P. (2005). Experimental observation of the quantum Hall effect and Berry's phase in graphene. Nature, 438(7065), 201-204.

[25] Wallace, P. R. (1947). The band theory of graphite. Physical Review, 71(9), 622.

[26] Mak, K. F., Ju, L., Wang, F., & Heinz, T. F. (2012). Optical spectroscopy of graphene: From the far infrared to the ultraviolet. Solid State Communications, 152(15), 1341-1349.

[27] Wehling, T. O., Grigorenko, I., Lichtenstein, A. I., & Balatsky, A. V. (2008). Phonon-mediated tunneling into graphene. Physical review letters, 101(21), 216803.

[28] Peres, N. M. R. (2010). Colloquium: The transport properties of graphene: An introduction. Reviews of Modern Physics, 82(3), 2673.

[29] Kuzmenko, A. B., Van Heumen, E., Carbone, F., & Van Der Marel, D. (2008). Universal optical conductance of graphite. Physical review letters, 100(11), 117401.

[30] Ando, T., Zheng, Y., & Suzuura, H. (2002). Dynamical conductivity and zero-mode anomaly in honeycomb lattices. Journal of the Physical Society of Japan, 71(5), 1318-1324.

[31] Mak, K. F., Shan, J., & Heinz, T. F. (2011). Seeing many-body effects in single-and few-layer graphene: observation of two-dimensional saddle-point excitons. Physical review letters, 106(4), 046401.

[32] Gogoi, P. K., Santoso, I., Saha, S., Wang, S., Neto, A. H. C., Loh, K. P., ... & Rusydi, A. (2012). Optical conductivity study of screening of many-body effects in graphene interfaces. EPL (Europhysics Letters), 99(6), 67009.

[33] Santoso, I., Singh, R. S., Gogoi, P. K., Asmara, T. C., Wei, D., Chen, W., ... & Rusydi, A. (2013). Tunable optical absorption and interactions in graphene via oxygen plasma. arXiv preprint arXiv:1307.1358.